Simulation of Aqueous Solutes Using the Adaptive Solvent-Scaling (AdSoS) Scheme

Working Paper

Author(s):
Kubincová, Alzbeta; Riniker, Sereina; Hünenberger, Philippe Henry

Publication date:
2023-11-22

Permanent link:
https://doi.org/10.3929/ethz-b-000644904

Originally published in:
ChemRxiv, https://doi.org/10.26434/chemrxiv-2023-f1fqx

Funding acknowledgement:
175944 - A Combinatorial Computational Chemistry Approach to Force-Field Development (SNF)

Simulation of Aqueous Solutes Using the Adaptive Solvent-Scaling (AdSoS) Scheme

Alžbeta Kubincová,[1] Sereina Riniker,[1] and Philippe H. Hünenberger[1]

Laboratory of Physical Chemistry, ETH Zurich, Vladimir-Prelog-Weg 2, 8093 Zurich, Switzerland

(*Electronic mail: phil@igc.phys.chem.ethz.ch)

(Dated: 8 November 2023)

The Adaptive Solvent-Scaling (AdSoS) scheme [J. Chem. Phys. 155 (2021) 094107] is an adaptive-resolution approach for performing simulations of a solute embedded in a fine-grained (FG) solvent region surrounded by a coarse-grained (CG) solvent region, with a continuous FG↔CG switching of the solvent resolution across a buffer layer. Instead of relying on a distinct CG solvent model, AdSoS is based on CG models defined by a dimensional scaling of the FG solvent by a factor s, accompanied by the s-dependent modulation of its mass and interaction parameters. The latter changes are designed to achieve an isomorphism between the dynamics of the FG and CG models, and to preserve the dispersive and dielectric solvation properties of the solvent with respect to a solute at FG resolution. As a result, the AdSoS scheme minimizes the thermodynamic mismatch between the different regions of the adaptive-resolution system. The present article generalizes the scheme initially introduced for a pure atomic liquid in slab geometry to more practically relevant situations involving: (*i*) a molecular dipolar solvent (*e.g.* water); (*ii*) a radial geometry (*i.e.* spherical rather than planar layers); and (*iii*) the inclusion of a solute (*e.g.* water molecule, dipeptide, ion or ion pair).

I. INTRODUCTION

Classical molecular dynamics (MD) simulations carried out at fully atomistic resolution are computationally intensive, resulting in limitations in terms of accessible system sizes and time scales. One approach to reduce the computational cost relies on the use of coarse-grained (CG) models,[1–13] where the resolution of the solute and/or solvent is reduced from individual atoms to beads representative of small atom groups. An early example of this approach is the use of united-atoms to represent the aliphatic CH_n groups as a single interaction site.[14] United-atoms are often employed in models that are otherwise at fully atomistic resolution, and the word fine-grained (FG) will be used here to denote models at (united-)atom resolution.

Numerous multi-scaling methods[1,2,11,15–19] have also been developed to combine FG and CG representations within the same calculation, with the goal of striking a favorable balance between the higher accuracy of the FG resolution and the higher efficiency of the CG resolution. Among these, mixed- or adaptive-resolution approaches are based on FG and CG regions coexisting spatially in the same system. Considering a single solute in a given solvent (*e.g.* hydrated macromolecule or lipid bilayer), a particularly interesting combination of this type relies on embedding the FG solute in a FG solvent region itself surrounded by a CG solvent region, the two regions being separated by a buffer layer permitting FG↔CG mixing or interconversion.[16,20–30] On the one hand, this combination provides a much more accurate FG treatment of short-range solvation compared to a direct solvation of the FG solute in the CG solvent[20,24,25,31–41]. On the other hand, it is expected to retain most of the efficiency gain associated with a CG resolution of the solvent considering that solvent-solvent interactions in the bulk are typically determinant in terms of computational costs. Another key advantage of this setup is that it only requires the design of a CG model for the solvent, which is generally much easier than the corresponding task for the solute. In practice, the computational gain will depend on the number N_G of FG molecules mapped to a single CG solvent bead (level of graining), and on the number N_S of interaction sites associated with the CG bead. In the context of CG water models[4,42–54], typical values of N_G and N_S are in the ranges 1-10 and 1-3, respectively.

In the mixed-resolution variant, the FG and CG molecules are allowed to mix in the buffer layer.[20–22,24–26] The extent of mixing is typically controlled by means of attractive and/or repulsive restraints relative to the solute. In the adaptive-resolution variant,[27–30] the FG and CG particles interconvert into each other as they cross the buffer layer. When N_G is one, this can be achieved by

morphing, *i.e.* interpolating between the interaction potentials or forces of the FG and CG models using a coupling variable that varies continuously with the position across the buffer layer. When $N_G > 1$, the transformation maps unequal numbers of molecules, and may be combined with a bundling scheme that associates clusters of nearby FG molecules to a single CG bead.[23,30,55–58]

The most popular adaptive-resolution schemes relying on morphing across a fixed buffer layer are the Adaptive Resolution Simulation (AdResS) scheme[59–65] and its Hamiltonian (H-AdResS) variant[19,23,27–30,55,66–69] (see also Refs. 16,70–77 for related approaches). Here, the buffer region is defined by an internal (FG to buffer) and an external (buffer to CG) boundary, both of which are fixed in space relative to the solute. Between the two boundaries, the resolution of a solvent particle changes progressively according to a switching parameter λ that is a continuous function of position, and evaluates to 1 (full FG) and to 0 (full CG) at the inner and outer boundaries, respectively. The switching is applied to the forces in AdResS (thereby enforcing the validity of Newton's third law) or to the Hamiltonian in H-AdResS (thereby enforcing the conservation of the total energy).

Note that the latest version of AdResS,[78,79] which we will refer to here as TR-AdResS, differs in two respects from the above description (see *e.g.* Fig. 1 in Ref. 78): (*i*) the CG molecules are replaced by so-called tracer (TR) particles that are exempt of non-bonded interactions and only subject to an effective pre-calibrated one-particle force that maintains a correct homogeneous particle density in the TR-region; (*ii*) the progressive resolution change is replaced by an abrupt transition from the AT level at the TR boundary, the buffer region now corresponding to normal AT molecules with density anomalies corrected using a similar effective one-particle force. In recent applications, the TR-AdResS scheme has also been used to handle non-equilibrium situations[80] or to bridge atomistic systems with continuum hydrodynamic reservoirs.[81]

Adaptive-resolution schemes relying on a buffer layer with FG↔CG solvent interconversion (as well as the closely related mixed-resolution schemes) have three main shortcomings[82]: (*i*) for a given choice of solvent, they rely on a unique graining level N_G that must be selected prior to the design of a CG model; (*ii*) this CG model must be parametrized, which is a non-trivial task, or an existing model must be taken from the literature; and (*iii*) the imperfect compatibility between the FG and CG models generally induces boundary artifacts. The latter artifacts[64,65] can be eliminated by application of different types of corrections, including a biasing of the chemical potential[61,67–69,76] or the application of a thermodynamic force along the density gradient.[62,63,83] Note that AdResS can also be used in a grand-canonical fashion, where the CG model is replaced

by non-interacting tracer particles.[84,85]

In a recent article,[82] we introduced a simple and elegant approach to derive CG models of arbitrary graining levels directly based on a given FG solvent model. The mapping involves a scaling of the spatial dimensions by a factor s, with the FG model corresponding to an s-value of one, along with a corresponding s-dependent adjustment of the force-field parameters of the solvent molecule. The latter changes are designed to achieve an isomorphism between the dynamics of the FG and CG models, and to preserve the dispersive and dielectric solvation properties of the solvent with respect to a solute at FG resolution. For a given value of s, the CG model thus represents a "blown up" version of the FG model with a graining level $N_G = s^3$. It involves the same number N_S of interaction sites in the same angular geometry, but different bond lengths as well as different atomic masses and interaction parameters. Note that a "blown-up" water-like aspect has also been selected empirically in a number of existing three-site CG water models[47,52,53].

The solvent-scaling approach offers a number of advantages compared to traditional coarse-graining: (*i*) the CG parameters are immediately related to those of the FG model (no need to parametrize a distinct CG model); (*ii*) nearly ideal mixing is expected for CG variants with similar s-values (ideal mixing holding in the limit of identical s-values); (*iii*) the solvent relaxation timescales should be preserved (no dynamical acceleration typical for coarse-graining[86–88]); (*iv*) the graining level N_G can be chosen arbitrarily (and need not be an integer); and (*v*) in an adaptive-resolution scheme, this level can be varied continuously as a function of the position (without requiring a bundling mechanism), and the variation occurs at a constant number of particles per molecule (no occurrence of fractional degrees of freedom[89,90] in the buffer layer).

Based on these ideas, we proposed a scheme called Adaptive Solvent-Scaling (AdSoS), where the parameter s governing the scaling of the solvent varies as a function of the position of the molecule in space. Starting from an s-value of one in the FG region close to the solute, the value of s is progressively increased across a SG region (buffer layer) to reach a value $s_{\max}$, which is then kept constant in the long-range CG region. By construction, the AdSoS scheme minimizes the thermodynamic mismatch between the different regions of the adaptive-resolution system, leading to a nearly homogeneous scaled number density $s^3\rho$ for the solvent. Residual density artifacts in and at the surface of the boundary layer can easily be eliminated by means of a grid-based correction potential constructed in a preliminary pure-solvent simulation.

When comparing AdSoS to the TR-AdResS scheme,[78,79] we note the three following points. For large systems, the TR-representation in AdResS (which only involves one-particle forces) will

be less expensive than the CG-representation in AdSoS (which still relies on pairwise forces). However, AdSoS also presents two advantages. First, the progressive transition FG↔SG↔CG, as determined by the continuous position-dependent scaling parameter s, is smooth, *i.e.* it involves no non-conservative forces. This is not the case in TR-AdResS, where the sudden insertion of TR-particles into the AT region may induce very large forces, which need to be capped (truncated). Second, in TR-AdResS, the TR region does not interact at all with the AT region, *i.e.* it provides no solvation contribution to a solute located in this region. This is not the case for AdSoS, where the scaled solvent in the SG and CG regions provide (by construction of the scaling) appropriate solvation contributions to such a solute (see Fig. 1 in Ref. 82). In other words, the CG-region of AdSoS extends the solvation range, whereas the corresponding TR-region in AdResS only functions as a (computationally less expensive) particle reservoir at the correct density for the definition of an open system.

The original article[82] provided the theory along with an initial application of AdSoS considering a pure monoatomic solvent (no solute) in a slab geometry. The goal of this article is to extend the AdSoS scheme to more practically relevant situations, involving: (i) a molecular dipolar solvent (*e.g.* water); (ii) a radial geometry (*i.e.* spherical rather planar layers); and (iii) the actual inclusion of a solute (*e.g.* solute water molecule, dipeptide, ion, or ion pair).

II. THEORY

The solvent-scaling approach for the definition of CG solvent models with arbitrary graining levels and the implementation of this approach into an adaptive-resolution scheme have been described in details in Ref. 82. This information is only briefly summarized below, and the reader is referred to the original publication for more details.

In the generalization from an atomic to a molecular solvent, the choice is made to apply a common value of the scaling factor s (as determined by the position of a specified reference point in the molecule) to all atoms within a given molecule. This choice is considered more appropriate than the use of distinct scaling factors for the different atoms (determined by their own positions) because it is consistent with a linear scaling of the interatomic distances (bonds) that preserves the angular structure (bond angles, dihedral angles) as well as the electroneutrality (zero net charge) of the solvent molecule upon scaling. For simplicity, it is also assumed that the selected FG solvent model is entirely rigid (no intramolecular interactions), and that its specification is complemented

by the selection of a reference atom (*e.g.* oxygen atom for a rigid water model).

A. AdSoS Scheme for a Solvent Molecule

In the solvent-scaling approach, the CG representation of a given FG solvent model is defined as a "blown up" version of this FG model. The transformation is controlled by the scaling parameter s, which defines the amount of (isotropic) stretching in the effective size of the molecule along each Cartesian dimension. The value $s = 1$ corresponds to the original FG model, while values $s > 1$ lead to a continuum of CG models with increasing graining levels $N_G = s^3$. In the context of a molecular solvent, the number N_S of interaction sites is preserved as well as their angular geometry, while the effective size is increased *via* a scaling of the bond lengths and van der Waals radii. The parameter scaling also affects the atomic masses and partial charges.

As detailed in Ref. 82, the scalings of the different physical quantities Q (force-field parameters, configurational variables, thermodynamic observables) follow equations of the form

$$Q(s) = s^{n_Q} Q^*, \tag{1}$$

where Q^* refers to the property of the unscaled model (corresponding to $s = 1$). The exponents n_Q associated with the most important physical quantities are summarized in Table I.

TABLE I: Dependence of various physical quantities on the scaling factor upon solvent-scaling. The exponent n_Q controlling the scaling of a property Q based on the scaling factor s (Eq. 1) is reported for the most important quantities. The force-field parameters considered are atomic mass (m), reference bond lengths (collectively noted b_o), reference bond angles or dihedral angles (collectively noted θ_o), Lennard-Jones parameters (c_6 and c_{12}), atomic partial charge (q), and reaction-field permittivity (ε_{RF}). The Lennard-Jones parameters c_6 and c_{12} correspond to single-atom square-root dispersion and repulsion coefficients, respectively. Their products determine the magnitude of the corresponding interactions for two given atoms (geometric-mean combination rule[91,92]). The configurational variables considered are time (t), coordinate (r), volume (V), velocity (v), momentum (p), and force (F). The thermodynamic observables considered are the Hamiltonian ($\mathcal{H}$), kinetic energy ($\mathcal{K}$), potential energy ($\mathcal{U}$), virial ($\mathcal{W}$), temperature (T), pressure (P), number density (ρ), isothermal compressibility (κ), and relative dielectric permittivity (ε).

n_Q	Parameter	Configuration	Observable
-3			ρ, P
-2	m		
-1		F, p	
0	θ_o, ε_{RF}	t	$\mathcal{H}, \mathcal{U}, \mathcal{K}, \mathcal{W}, T, \varepsilon$
$1/2$	q		
1	b_o	r, v	
3	c_6	V	κ
6	c_{12}		

In the AdSoS scheme[82], the scaling factor s_i assigned to an atom i is adapted on-the-fly based on the position vector $\boldsymbol{R}_I$ of the reference atom within molecule I which atom i belongs to, *i.e.*

$$s_i = s(\boldsymbol{R}_I) \ . \tag{2}$$

In practice, the value of s is progressively increased from one (in the immediate vicinity of the FG solute) to a maximal value $s_{\max}$ (sufficiently far from the solute). The solute itself is entirely described at the FG level ($s = 1$). Considering the scalings of Eq. (1) and Table I for the force-field parameters, it follows that the bond lengths in the solvent molecule are amplified by s_I with no change in the angular geometry. Concerning the interaction parameters α_i of solvent atom i (mass

m, partial charge q, square-root dispersion coefficient c_6 and square-root repulsion coefficient c_{12}), the scaling is given by

$$\alpha_i(s_i) = s_i^{n_\alpha} \alpha_i^* \ , \tag{3}$$

with $n_m = -2$, $n_q = 1/2$, $n_{c_6} = 3$, $n_{c_{12}} = 6$, and where s_i refers to the s_I value of the solvent molecule to which atom i belongs. The same equation can also be used for the solute atoms, with the convention that $s_i = 1$ (FG level) in this case.

For the configurational variables and the thermodynamic observables, the scalings of Eq. 1 only hold exactly in the context of pure-solvent systems with a homogeneous s-value[82]. However, they are still expected to hold approximately for a pure solvent in the AdSoS setup, provided that the s-gradients within the system are sufficiently low. Note, in particular, that the energetic quantities (including the temperature), the relaxation times, and the dielectric permittivity are all invariant upon scaling.

The AdSoS Hamiltonian for a solute-solvent system of N atoms reads

$$\mathcal{H}(\boldsymbol{r},\boldsymbol{p}) = \mathcal{K}(\boldsymbol{r},\boldsymbol{p}) + \mathcal{U}_{\text{cov}}(\boldsymbol{r}) + \mathcal{U}_{\text{ele}}(\boldsymbol{r}) + \mathcal{U}_{\text{vdw}}(\boldsymbol{r}) \ , \tag{4}$$

where $\boldsymbol{r}$ and $\boldsymbol{p}$ are the $3N$-dimensional atomic Cartesian position and momentum vectors, respectively, $\mathcal{K}$ is the kinetic energy, and $\mathcal{U}_{\text{cov}}$, $\mathcal{U}_{\text{ele}}$ and $\mathcal{U}_{\text{vdw}}$ are the covalent, electrostatic, and van der Waals potential energies, respectively. The kinetic energy, which depends here on position (*via* s_i) as well as on momentum, is given by

$$\mathcal{K}(\boldsymbol{r},\boldsymbol{p}) = \sum_i^N \frac{\boldsymbol{p}_i^2}{2m_i(s_i)} \ . \tag{5}$$

In the context of a rigid solvent model (no intramolecular interactions), the covalent term $\mathcal{U}_{\text{cov}}$ only involves the solute. Since the latter is represented at the FG level, this term is not affected by the solvent-scaling scheme. The electrostatic term $\mathcal{U}_{\text{ele}}$ corresponds to Coulomb[93] interactions with a reaction-field correction[94,95], and is given by

$$\mathcal{U}_{\text{ele}}(\boldsymbol{r}) = \frac{1}{4\pi\varepsilon_o} \sum_i^N \sum_{j>i}^N q_i(s_i) q_j(s_j) \left(\frac{1}{r_{ij}} + \frac{\varepsilon_{RF}-1}{1+2\varepsilon_{RF}} \frac{r_{ij}^2}{R_c^3} - \frac{3\varepsilon_{RF}}{1+2\varepsilon_{RF}} \frac{1}{R_c} \right) , \tag{6}$$

where $\boldsymbol{r}_{ij} = \boldsymbol{r}_i - \boldsymbol{r}_j$ is the (minimum-image) vector connecting atom j to atom i, ε_o is the permittivity of vacuum, ε_{RF} is the reaction-field permittivity, and R_c is the cutoff distance. The van der Waals term $\mathcal{U}_{\text{vdw}}$ corresponds to a Lennard-Jones function[96] with a geometric-mean combination

rule[91,92], and is given by

$$\mathcal{U}_{\mathrm{vdw}}(\boldsymbol{r}) = \sum_{i}^{N} \sum_{j>i}^{N} \left(c_{12,i}(s_i)\, c_{12,j}(s_j)\, r_{ij}^{-12} - c_{6,i}(s_i)\, c_{6,j}(s_j)\, r_{ij}^{-6} \right) . \tag{7}$$

Eqs. (3)-(7), together with a specification for the function s in Eq. 2, provide the framework of the AdSoS scheme.

The Hamiltonian of Eq. (4) depends on the atomic positions not only explicitly, but also implicitly, *via* the position-dependence of s_i. The force on an atom i is thus given by

$$\boldsymbol{F}_i = -\frac{\partial \mathcal{H}}{\partial \boldsymbol{r}_i} = -\left(\frac{\partial \mathcal{H}}{\partial \boldsymbol{r}_i}\right)_{s_i} - \left(\frac{\partial \mathcal{H}}{\partial s_i}\right)_{\boldsymbol{r}_i} \frac{\mathrm{d}s_i}{\mathrm{d}\boldsymbol{r}_i} . \tag{8}$$

The first term represents the physical force. For the pairwise terms $\mathcal{U}_{\mathrm{ele}}$ and $\mathcal{U}_{\mathrm{vdw}}$ this force acts along the vector connecting the two atoms involved. The second term represents a so-called drift force.[28,66,97,98] It is only relevant for solvent molecules in regions where s varies, and acts in the direction of the s-gradient. Expressions for the forces associated with the terms of Eqs. (5)-(7) are provided in Suppl. Mat. Section S1.1.

The inclusion of the drift force in the dynamics of AdSoS is essential to prevent the occurrence of density artifacts. As discussed previously[82], this force compensates on average for the thermodynamic driving force associated with a heterogeneous pressure in the system, which results from the fact that the pressure in a solvent region at scaling s is given by $P(s) = s^{-3}P^*$. This pressure heterogeneity is necessary because the pressure $s^{-3}P^*$ is the one that leads to the correct solvent number density $\rho(s) = s^{-3}\rho^*$. Note that this compensation only holds in the limit of a sufficiently large number of molecules and of sufficiently low s-gradients in the system.

Owing to the time-dependence of the masses (*via* the position-dependence of s_i), the leap-frog integrator[99] must be adapted to the AdSoS situation. The adjusted version can be derived directly from the Hamiltonian equations,[82,100] leading to

$$\begin{aligned} \boldsymbol{v}_i(t+\Delta t/2) &= \left(\frac{s_i(t)}{s_i(t-\Delta t)}\right)^2 \boldsymbol{v}_i(t-\Delta t/2) + \frac{\boldsymbol{F}_i(t)}{m_i(t)}\Delta t \\ \boldsymbol{r}_i(t+\Delta t) &= \boldsymbol{r}_i(t) + \boldsymbol{v}_i(t+\Delta t/2)\Delta t, \end{aligned} \tag{9}$$

where $\boldsymbol{v}_i$ is the velocity of atom i and Δt the integration step. The adaptation of the SHAKE algorithm[101] for enforcing a rigid solvent geometry in the AdSoS scheme is outlined in Suppl. Mat. Section S1.2.

In principle, the AdSoS scheme does not introduce any non-conservativeness *per se*, so that it should by default sample a microcanonical (NVE) ensemble in the absence of a thermostat. In

practice, however, the use of finite values for the integration timestep and for the non-bonded cutoff will lead to energy drifts. These are removed by the thermostat in the canonical (NVT) ensemble, and one could easily imagine a variant using an "ergostat" (*i.e.* a heat exchange designed to maintain the total energy of the system) that would sample the microcanonical one.

B. System Geometries

As illustrated in Figure 1, two different system geometries are considered for the implementation of AdSoS, namely slab and radial (spherical) geometries. Both involve a computational box simulated under periodic boundary conditions. For simplicity, the discussion is restricted here to a rectangular box for the slab geometry and to a cubic box for the spherical geometry. The three Cartesian directions $\alpha = x, y, z$ are associated with unit vectors $\boldsymbol{e}_\alpha$ and box-edge lengths L_α. In slab geometry, the special direction is the z-direction. In spherical geometry, the edge length of the cubic box is denoted L.

In both cases, the box is partitioned into three regions: (*i*) the FG region, which contains the solute surrounded by unscaled solvent molecules; (*ii*) the SG region, where the scaling factor is progressively increased from 1 to $s_{\max}$; and (*iii*) the CG region, where the solvent is homogeneously scaled at $s_{\max}$. The widths of these regions are denoted d_{FG}, d_{SG}, and d_{CG}, respectively. In the slab case, the system includes two SG regions of widths d_{SG}, so that $L_z = d_{FG} + 2d_{SG} + d_{CG}$. In the spherical case, d_{FG} refers to the diameter of the FG region, and d_{CG} represents twice the distance between the start of the CG region and the closest box wall (or, equivalently, the minimum width of the CG region *via* periodicity), so that, here as well, $L = d_{FG} + 2d_{SG} + d_{CG}$. The equations below assume that the representative periodic copies of the solvent molecules are selected at minimum-image positions relative to the center of the computational box.

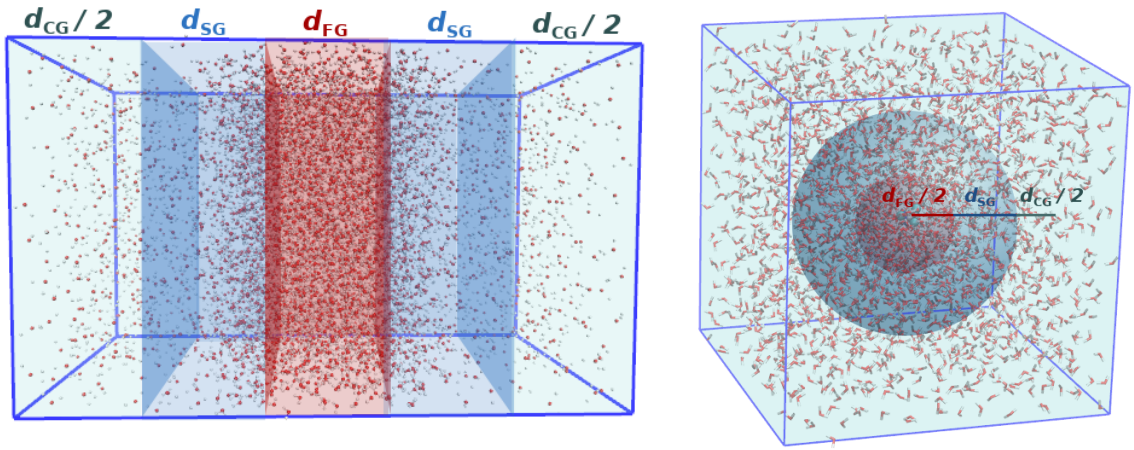

FIG. 1: Schematic representation of the box partitioning in AdSoS for the slab (left) and spherical (right) geometries. The FG region is marked in red, the SG region(s) in dark blue, and the CG region in light blue. The widths d_{FG}, d_{CG} and d_{SG} of the different regions are also indicated. The scaling factor s is modulated according to Eqs. (12) and (13).

In both geometries, an absolute position vector $\boldsymbol{r}$ within the box is converted to a unitless relative position vector $\boldsymbol{a}$ that will serve to define the s-value and its gradient. In slab geometry, the vector $\boldsymbol{a}$ is defined as

$$\boldsymbol{a}(\boldsymbol{r}) = L_z^{-1}\left(r_z - \frac{L_z}{2}\right)\boldsymbol{e}_z \quad \text{(slab)} \tag{10}$$

where $\boldsymbol{e}_z$ is a unit vector along the z-direction. The magnitude of $\boldsymbol{a}$ is zero in the $(x, y, L_z/2)$ plane and increases with the distance from this plane up to a maximum of $1/2$. The direction of $\boldsymbol{a}$ is along $-\boldsymbol{e}_z$ at the left and $+\boldsymbol{e}_z$ at the right of the plane. In spherical geometry, the vector $\boldsymbol{a}$ is defined as

$$\boldsymbol{a}(\boldsymbol{r}) = L^{-1}\sum_{\alpha=x,y,z}\left(r_\alpha - \frac{L}{2}\right)\boldsymbol{e}_\alpha \quad \text{(spherical)}\,, \tag{11}$$

where $\boldsymbol{e}_z$ is a unit vector along direction α (where $\alpha = x$, y or z). The magnitude of $\boldsymbol{a}$ is zero at the box center $(L_x/2, L_y/2, L_z/2)$ and increases with the distance from this point up to a maximum of $3^{1/2}/2$ at the cube corner. The direction of $\boldsymbol{a}$ is always radial from the box center and oriented towards the outside.

In both geometries, the relative distance a is defined as the norm of $\boldsymbol{a}$. The dependence of the scaling factor on the position $\boldsymbol{r}$ within the box is then formulated in terms of this relative distance

as

$$s(\boldsymbol{r}) = w(a(\boldsymbol{r})) \tag{12}$$

with

$$w(a) = \begin{cases} 1 & a \leq \frac{1}{2}\delta_{\mathrm{FG}} \\ 1 + (s_{\max} - 1)\sin^2\left[\frac{\pi(a - \frac{1}{2}\delta_{\mathrm{FG}})}{2\delta_{\mathrm{SG}}}\right] & \frac{1}{2}\delta_{\mathrm{FG}} < a < \frac{1}{2}\delta_{\mathrm{FG}} + \delta_{\mathrm{SG}} \\ s_{\max} & a \geq \frac{1}{2}\delta_{\mathrm{FG}} + \delta_{\mathrm{SG}}. \end{cases} \tag{13}$$

where δ_X (with X = FG, CG or SG) is equal to d_X/L_z in slab geometry or to d_X/L in spherical geometry. This functional form is selected to provide a smooth transition in the SG region (continuously differentiable at the boundaries). The gradient of the scaling function can be formulated based on Eqs. 12 and 13 using the chain rule, namely

$$\frac{\mathrm{d}s}{\mathrm{d}\boldsymbol{r}} = \frac{\mathrm{d}w}{\mathrm{d}a}\frac{\mathrm{d}a}{\mathrm{d}\boldsymbol{r}} \tag{14}$$

where the derivative of a is obtained from Eqs. (10) or (11).

C. Correction Potentials

The AdSoS setup is designed to keep the thermodynamic mismatches in the system to a minimum by imposing near-ideal mixing properties for molecules at comparable s-values, a smooth continuous change of the s-value with position and an appropriate pressure heterogeneity enabled by the drift force. However, variations of s may still cause artifacts, which are expected to become increasingly pronounced for high s-gradients. Additional causes may include: (*i*) the implicit use of an *ad hoc* geometric-mean rule to combine the s_i and s_j factors within the pairwise interactions (Eq. (6) and (7)); (*ii*) specific close-range packing and orientation alterations between the solvent molecules in (or close to) regions presenting s-variations; and (*iii*) the use of cutoff truncation in the calculation of the non-bonded interactions. In the context of an atomic solvent[82], possible artifacts only concern the density, and affect nearly exclusively the SG region as well as the FG-SG and SG-CG interfaces. In the context of a molecular solvent, one also has to consider the possibility of artifacts in the orientation of the solvent molecules. If the solvent is polar (*e.g.* water), this may result in an erroneous solvent polarization around the solute. In practice, both types of artifacts are expected to remain limited in the case of sufficiently low s-gradients, and residual

effects can be corrected by application of positional (for the density) and orientational (for the polarization) grid-based correction potentials. These potentials should be calibrated in the absence of a solute, *i.e.* in the situation where solvent homogeneity and isotropy are expected, and then assumed to be portable from system to system, *i.e.* applicable irrespective of the solute.

In practice, these correction potentials are constructed using the local-elevation umbrella-sampling (LEUS) approach,[102] where they are represented as a weighted sum of local basis functions. A first local-elevation[103] (LE) phase involves the non-equilibrium build-up of the correction potential. A second umbrella-sampling (US) phase[104] involves the equilibrium sampling of the system using a frozen correction potential. Note that these potentials are expected to be specific to a given AdSoS setup, *i.e.* system geometry, choice of solvent, value of $s_{\max}$, sizes of the box compartments, and choice of the s-function. Here, cubic B-splines are used as basis functions,[105,106] namely

$$G(x) = \begin{cases} x^2(|x|-2)/2+2/3 & 0 \leq |x| \leq 1, \\ (2-|x|^3)/6 & 1 \leq |x| \leq 2 \\ 0 & \text{otherwise .} \end{cases} \tag{15}$$

The positional correction potential to eliminate density artifacts is constructed along the unitless relative distance a for the corresponding system geometry (Eqs. (10) and (11)). The distance coordinate is discretized using a one-dimensional grid of points $k = 1...K$. Each grid point is the origin of a kernel function G (Eq. 15). The corresponding potential energy function U_ρ is applied to the reference point $\boldsymbol{R}_I$ of each solvent molecule I and reads

$$U_\rho(\boldsymbol{r}) = b_\rho \sum_I^{N_I} \sum_k^K w_{\rho,k} G\left(\frac{a(\boldsymbol{R}_I) - a_k}{\omega_\rho \Delta}\right), \tag{16}$$

where N_I is the number of solvent molecules, b_ρ is a force constant (determining the build-up rate), a_k and $w_{\rho,k}$ are the position and weight associated with grid point k, ω_ρ is the kernel width in grid units and Δ is the grid spacing. The latter is given by $\Delta = K^{-1} a_{\max}$, where $a_{\max}$ is 1/2 in slab geometry and $3^{1/2}/2$ in spherical geometry. There are three main differences in the procedure compared to the standard LEUS scheme[102]. First, the factor ω_ρ is introduced which, when differing from 1, permits to make the correction potential smoother. Second, all solvent molecules are coupled to the same (one-dimensional) correction potential. Third, a molecule I at grid point k increments the corresponding weight $w_{\rho,k}$ by $v_k^{-1} s_I^3$ (instead of one), where v_k is the volume of

bin k

$$v_k = \int_0^{\boldsymbol{L}} \left[\Theta(a(\boldsymbol{r}) - k\Delta) - \Theta(a(\boldsymbol{r}) - (k+1)\Delta)\right] \mathrm{d}\boldsymbol{r}, \tag{17}$$

with Θ being the Heaviside step function. These volumetric factors are used for the normalization of the density at a given grid point. In slab geometry, v_k = 1/2 for $k = 1$ and $k = K$, or 1 otherwise. In spherical geometry, $v_k = 4\pi/3\left[((k+1)\Delta)^3 - (k\Delta)^3\right]$ if $(k+1)\Delta \leq 1/2$, or is evaluated as the result from a cube-sphere intersection for $(k+1)\Delta > 1/2$ (solved numerically). The algorithms for constructing and applying the correction potential of Eq. (16) are outlined in Suppl. Mat. Section 1.3.

The orientational correction potential U_μ to eliminate polarization artifacts is applied to all solvent atoms $i = 1...N$ with a charge-weighting

$$U_\mu(\boldsymbol{r}) = \sum_i^N q_i \Phi_{\mu,i}(\boldsymbol{r}_i), \tag{18}$$

where $\Phi_{\mu,i}$ represents an electric potential acting on atom i

$$\Phi_{\mu,i}(\boldsymbol{r}_i) = b_\mu \sum_k^K w_{\mu,k} G\left(\frac{a(\boldsymbol{r}_i) - a_k}{\omega_\mu \Delta}\right) . \tag{19}$$

In practice, the biasing potential U_μ is constructed as follows. First, the local electric field component e_k along $\boldsymbol{a}$ in each bin k is calculated according to

$$e_k = \sum_I^{N_I} \mu_r \left[\Theta(a(\boldsymbol{r}) - k\Delta) - \Theta(a(\boldsymbol{r}) - (k+1)\Delta)\right] , \tag{20}$$

where μ_r is the projection of the molecular dipole $\boldsymbol{\mu}_I$ onto the vector $\boldsymbol{a}$,

$$\mu_r = \frac{\boldsymbol{\mu}_I \cdot \boldsymbol{a}(\boldsymbol{R}_I)}{\mu_I \cdot a(\boldsymbol{R}_I)} . \tag{21}$$

The weights $w_{\mu,k}$ are then incremented by minus the integral of $e(r)$ between 0 and $k\Delta$ (which implies $w_{\mu,0} = 0$). In practice, the integration is carried out by linearly interpolating $e(r)$. The algorithms for constructing and applying U_μ are outlined in Suppl. Mat. Section 1.3.

In contrast to the LEUS approach, which relies on a damping of the build-up rate after each double-sweep of the entire range during the LE phase[102] (similar to well-tempered metadynamics[107]), the present scheme relies on a constant build-up rate in the LE phase (which leads to oscillations in the weights). The biasing potential for the US phase is then defined by averaging the weights over a certain period at the end of the LE phase.

III. METHODS

A. Computational Details

The AdSoS scheme was implemented into the GROMOS simulation program.[108] The solvent considered is water with the parameters of the simple point charge (SPC) model.[109] The molecule is entirely rigid, and its reference point was chosen to be the oxygen atom. The parameters for the different solutes considered were taken from the GROMOS 54A7 force field.[110]

The initial configurations for pure-liquid simulations were obtained by randomly placing M water molecules in the computational box. The number of molecules M was determined according to

$$M = \rho^* \int_0^{L_x} \int_0^{L_y} \int_0^{L_z} s^{-3}(x,y,z)\,\mathrm{d}x\,\mathrm{d}y\,\mathrm{d}z\,, \tag{22}$$

where $\rho^* = 32.5\ \mathrm{nm}^{-3}$ is the bulk number density of liquid water at 298.15 K and 1 bar, and s the scaling function defined by Eq. (12) (expressed here as a function of the position in the box).

Simulations in slab geometry were carried out for three possible choices of $s_{\max}$, namely 1.0, 1.5 and 2.0, corresponding to maximal graining levels N_G of 1.0, 3.375 and 8.0, respectively. They relied on a rectangular computational box with $L_z = 10$ nm containing M water molecules, with the partitioning $d_{\mathrm{FG}} = 2.0$ nm, $d_{\mathrm{SG}} = 2.0$ nm, and $d_{\mathrm{CG}} = 4.0$ nm (Fig. 1, left). For $s_{\max} = 1.0$ (FG reference system), the parameters were $L_x = L_y = 2.5$ nm and $M = 2031$. For $s_{\max} = 1.5$, they were $L_x = L_y = 4$ nm and $M = 2859$. For $s_{\max} = 2.0$, they were $L_x = L_y = 6$ nm and $M = 4890$.

Simulations in spherical geometry were carried out for two possible choices of $s_{\max}$, namely 1.0 and 2.0, corresponding to maximal graining levels N_G of 1.0 and 8.0, respectively. For the reference simulations with $s_{max} = 1$ (FG reference system), a small cubic box with edge length $L = 3$ nm containing $M = 877$ water molecules (FG/S) as well as a large cubic box with edge length $L = 8$ nm containing $M = 16640$ water molecules (FG) were considered. The AdSoS simulations relied on a cubic box with edge length $L = 8$ nm containing $M = 2732$ water molecules, with the partitioning $d_{\mathrm{FG}} = 2.0$ nm, $d_{\mathrm{SG}} = 2.0$ nm, and $d_{\mathrm{CG}} = 2.0$ (Fig. 1, right).

All simulations were carried out in the canonical (NVT) ensemble at 298.15 K using a weak-coupling thermostat[111] with a coupling time of 0.1 ps. The equations of motion were integrated using the modified Leap-frog scheme of Eq. (9) with a time step of 2 fs. The full rigidity of the water molecules was maintained using three distance constraints, enforced using the modified SHAKE algorithm[101] of Suppl. Mat. Sec. 1.2, applied with a relative geometric tolerance of

10^{-12} (chosen very small to avoid possible artifacts due to unequal noise levels at different scaling values). The non-bonded interactions were evaluated using charge-group truncation at a single-range cutoff distance R_c based on a pairlist updated every step. A reaction-field correction[94,95] was applied with a permittivity ε_{RF} set to 61.

The simulations were performed considering different cutoff radii R_c. For the FG reference systems ($s_{max} = 1$, both slab and spherical geometries), R_c was set to 1.2 or 1.4 nm (in some cases also 2.4 nm). In the scaled setup ($s_{\max}$ = 1.5 and 2.0), the values considered are R_c = 1.8 nm for $s_{\max} = 1.5$, and R_c = 2.0, 2.4 or 2.8 nm for $s_{\max} = 2.0$. The use of larger cutoff distances in the AdSoS setup (relative to the value of 1.4 nm typically employed in FG simulations with GROMOS) is rendered necessary by the linear scaling of distances (Table I), which leads to an effective interaction range reduced to $R_c/s_{\max}$ in the CG region. Note that even if raising R_c in proportion to $s_{\max}$ offsets the computational gain of AdSoS on a per molecule basis, the approach remains very advantageous because the number of solvent molecules is considerably reduced compared to a FG system filling the same volume.

Prior to production, the pure-liquid systems were subject to energy minimization with harmonic bonds (scaling of the force constant with s as $k_b(s) = s^{-2}k_b^*$), followed by a minimization with rigid bonds, and by 0.1 ns equilibration. Simulations without correction potentials were carried out for 10 ns, and the coordinates were written out every 100 steps. In spherical geometry, the oxygen atom of one reference water molecule was restrained to the center of the box with a harmonic force constant of 10^4 kJ mol^{-1} nm^{-2}.

The correction potentials for the solvent density (Eq. (16)) and orientation (Eq. (18)) were built up simultaneously over a LE phase of 20 ns. For the density bias, the force constant was set to $b_\rho = 10^{-2}$ kJ mol^{-1} and the kernel width ω_ρ in grid units to 1. The orientational bias relied on $b_\mu = 10^{-5}$ kJ mol^{-1} and ω_μ = 2. In slab geometry, the number of grid points was set to K = 51 ($\Delta = 0.1$ nm). In spherical geometry it was set to K = 73 ($\Delta = 0.096$ nm). The build-up was carried out separately for each distinct cutoff. In spherical geometry, it was carried out without the aforementioned position restraint on the central water molecule. The correction potentials used in the US phase were defined as averages over the last 15 ns of the LE phase, and the production runs of the US phase were carried out for 10 ns.

Simulations of a capped alanine dipeptide in spherical geometry were set up by replacing eight central water molecules in the pre-equilibrated cubic box. The C_α atom of the dipeptide was harmonically restrained to the box center with a force constant of 10^5 kJ mol^{-1} nm^{-2}. The system

was equilibrated for 0.1 ns. Sampling was then carried out for 100 ns with configurations written out every 500 steps. Simulations were carried out either without or with the correction potentials, which were constructed for the pure-water system.

Simulations of an ion in spherical geometry were set up by replacing the central water molecule in the pre-equilibrated cubic box with a Na^+ or a Cl^- ion. The ion was positionally constrained to the box center. Some simulations of ions with the same Lennard-Jones parameters but higher charge magnitudes (Na^{2+}, Na^{3+}, Cl^{2-} and Cl^{3-}) were carried out in a similar fashion. There also, the applied correction potential was constructed for the pure-water system. Sampling was carried out for 10 ns. Free-energy calculations also relied on 1 ns simulations performed with $|q| = 0.05$, 0.5 and 0.75 e ion charge (instead of the full charge).

To assess the distance distribution of aqueous ion pairs in the AdSoS setup, an additional ion was inserted into the FG region of the single-ion systems. While the first ion was positionally constrained to the box center, the second ion was subject to a half-harmonic flat-bottom distance restraint to the box center with a force constant of $3 \cdot 10^3$ kJ mol^{-1} nm^{-2} and an offset distance of 1 nm, in order to prevent it from leaving the FG region. Three combinations of ion pairs were considered: (i) Na^+ for both ions; (ii) Na^- for both ions; and (iii) Na^- as the center ion with Na^+ as the restrained ion. Only the charges of the ions were modified, their Lennard-Jones parameters were kept constant. The simulation settings were the same as for the single-ion simulations.

B. Analyses

Density profiles were calculated by time-averaging the scaled number density $s^3(z)\rho(z)$ in slab geometry (over the range $[0, L_z]$, *i.e.* with the FG region in the middle) and $s^3(r)\rho(r)$ in spherical geometry (over the range $[0, L/2]$, *i.e.* from the box center to the nearest box wall). Orientational profiles were calculated in the form of a time and space averages of molecular dipole moments $\mu_I(\boldsymbol{r})$ projected on $\boldsymbol{a}$.

Solute-solvent interaction energies were extracted from the simulated trajectories using the GROMOS++ program[112] `ene_ana`. Rotational relaxation times were calculated with the GROMOS++ program[112] `rot_rel`, which calculates the first and second Legendre polynomials of the

autocorrelation function of the OH bond

$$C_1(t) = \langle \boldsymbol{r}_{OH}(\tau) \cdot \boldsymbol{r}_{OH}(\tau + t) \rangle_\tau \approx \exp(-t/\tau_1^{OH}) \tag{23}$$

$$C_2(t) = \frac{1}{2}(3[C_1(t)]^2 - 1) \approx \exp(-t/\tau_2^{OH}) \tag{24}$$

The first and second rotational relaxation times τ_1^{OH} and τ_2^{OH} were estimated by fitting the slopes of the linearized forms of Eqs. (23) and (24), respectively.

Time series of the backbone ϕ and ψ dihedral angles in the alanine dipeptide were calculated using the GROMOS++ program[112] `tser`.

Single-ion solvation free energies ΔG^{corr} were calculated according to

$$\Delta G^{\text{corr}} = \Delta G^{\text{raw}} + \Delta G^{\text{extra}}. \tag{25}$$

Here, ΔG^{raw} is the free-energy difference obtained by integrating the electric potential Φ as a function of the charge q, from zero to the full ion charge q_{ion} (-1 for Cl^-, +1 for Na^+), namely

$$\Delta G^{\text{raw}} = \int_0^{q_{\text{ion}}} \Phi(q) \mathrm{d}q \qquad \text{where} \quad \Phi(q) = q^{-1} U_{\text{ele}} \, . \tag{26}$$

The term ΔG^{extra} is the free-energy correction described in Ref. 113, which consists of four components: (A) a correction term for the use of effective non-Coulombic electrostatic interactions inside and outside the cutoff; (B) a correction term for finite-size effects due to periodic boundary conditions; (C) a conversion factor from atom-based to molecule-based summation; and (D) a standard-state correction. A corrected electrostatic ion-solvent interaction energy $U_{\text{ele}}^{\text{corr}}$ was calculated according to

$$U_{\text{ele}}^{\text{corr}} = U_{\text{ele}}^{\text{CB}} + U_{\text{ele}}^{\text{CE}}, \tag{27}$$

where $U_{\text{ele}}^{\text{CB}}$ is the Coulomb component of the ion-solvent interaction energy, and $U_{\text{ele}}^{\text{CE}}$ is the contribution to the electrostatic energy from the dielectric continuum beyond the cutoff obtained from the Born equation[114]

$$U_{\text{ele}}^{\text{CE}} = -\frac{1}{4\pi\varepsilon_0}\left(1 - \frac{1}{\varepsilon_w}\right)\frac{q^2}{R_c}, \tag{28}$$

where $\varepsilon_w = 78.4$ is the static relative dielectric permittivity of water.

In the comparison of the polarization around multivalent ions with the Born model, the Born polarization $P(r)$ was calculated according to[115]

$$P_{\text{Born}}(r) = \frac{q_I}{4\pi r^2}\left(1 - \frac{1}{\varepsilon_{\text{SPC}}}\right) \, , \tag{29}$$

where q_I is the ion charge, and $\varepsilon_{\mathrm{SPC}} = 66.6$ the relative permittivity of the SPC water model.[109] Eq. (29) can be related to the radial distribution function $g(r)$ and the orientational profile $\mu_r(r)$ using

$$P_{\mathrm{sim}}(r) = \rho^* \mu^* g(r) \mu_r(r) \ , \tag{30}$$

where $\rho^* = 32.5\ \mathrm{nm}^{-3}$ is the bulk density and $\mu^* = 0.047\ e$ nm the dipole moment of SPC water model.

IV. RESULTS AND DISCUSSION

A. Density and Orientational Profiles for Pure Water

The density profiles for pure water in slab geometry are shown in Fig. 2 for the FG reference system ($s_{\mathrm{max}} = 1$) and the AdSoS setups ($s_{\mathrm{max}} = 1.5$ or 2). In the scaled systems without biasing potential (Fig. 2a), two kinds of density artifacts can be observed. The first kind consists of sinusoidal fluctuations in the SG region. These fluctuations do not decrease with increasing cutoff, and they can also be observed in the much simpler case of liquid argon with minimum-image cutoff.[82] This effect most likely results from the non-vanishing s-gradient in the SG region.

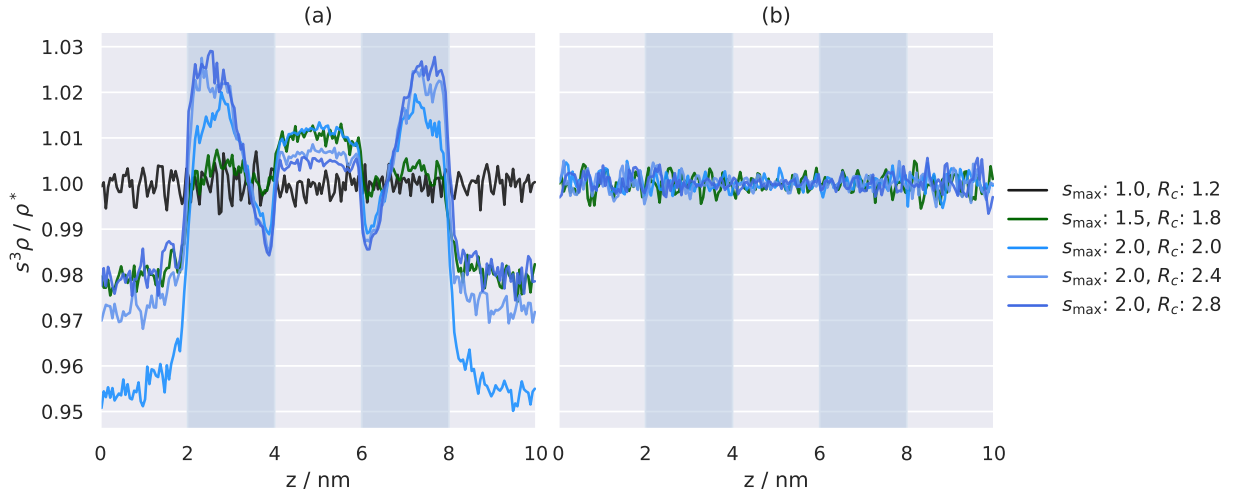

FIG. 2: Scaled density profiles $s^3\rho\,/\,\rho^*$ of a water box in slab geometry using AdSoS without (a) and with (b) an applied correction potential (longitudinal and orientational). The bulk number density is $\rho^* = 32.5\ \mathrm{nm}^{-3}$. The black line corresponds to the FG reference system ($s_{\max} = 1$). The green line shows the system with $s_{\max} = 1.5$. Blue lines represent systems with $s_{\max} = 2$ and three different cutoff values (R_c = 2.0, 2.4, or 2.8 nm). The shaded blue vertical strips mark the two SG regions surrounding the FG region.

The second kind of artifact is the density mismatch between the FG and CG regions. In contrast to the fluctuations in the SG region, the effect is reduced upon increasing the cutoff. A possible cause for this mismatch is that the effective cutoff $s^{-1}R_c$ is smaller for the CG than for the FG particles. Consequently, the FG atoms are experiencing stronger attractive dispersive interactions, leading to a higher density in the FG region. Note that these two artifacts remain limited in magnitude, with density variations on the order of $\pm$ 5% across the computational box.

Fig. 2b shows that both kinds of density artifacts can be eliminated by applying longitudinal and orientational biasing potentials. The corresponding time series of the weights $w_{\rho,k}$ during LE build-up and the final biasing potentials along a during US sampling are shown in the Suppl. Mat Figures S1 and S2, respectively. The LEUS weights are well converged after about 10 ns. The biasing potentials reflect the shape of the density profiles in Fig. 2a, and the peak-to-peak difference in U_ρ is about 1.5 - 2 kJ mol^{-1}, depending on $s_{\max}$ and R_c.

The orientational profiles of the water molecules for pure water in slab geometry are displayed in Fig. 3.

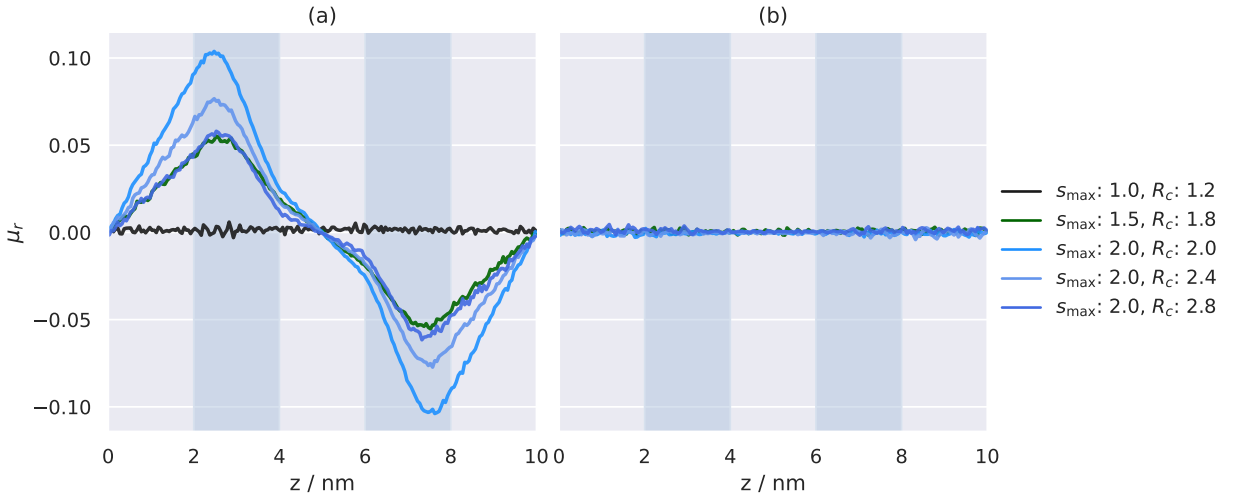

FIG. 3: Orientational profiles μ_r of a water box in slab geometry using AdSoS without (a) and with (b) an applied (longitudinal and orientational) correction potential. The quantity μ_r is defined by Eq. (21). The black line corresponds to the FG reference system ($s_{\max} = 1$). The green line shows the system with $s_{\max} = 1.5$. Blue lines represent systems with $s_{\max} = 2$ and three different cutoff values (R_c = 2.0, 2.4 or 2.8 nm). The shaded blue vertical strips mark the SG regions surrounding the FG region.

In the absence of a biasing potential (Fig. 3a), the effect of the FG-SG and SG-CG interface on the orientation of the water molecules has a longer range compared to its effect on the density, with the polarization in the FG and CG regions being highly affected. The magnitude of polarization artifacts increases with $s_{\max}$ (*i.e.* with the s-gradient in the SG region), and decreases upon increasing the cutoff R_c. This effect is largely independent from the density artifacts. Applying a correction potential for the density alone does not affect the polarization in a significant manner (data not shown). Figure 3a also suggests a preferential orientation of the hydrogen atoms towards the FG region in the center of the box. Fig. 3b shows that applying the longitudinal and orientational correction potentials results in a flat orientational profile, which is comparable to the FG reference. Time series of the weights $w_{\mu,k}$ and biasing electric potentials Φ_μ are provided in Suppl. Mat. Fig. S3 and S4, respectively.

The density and orientational profiles for water in spherical geometry are shown in Fig. 4. The density profile along the distance to the box center $d = aL$ is equivalent to a radial distribution function (RDF) around the water molecule which is positionally restrained at $d = 0$.

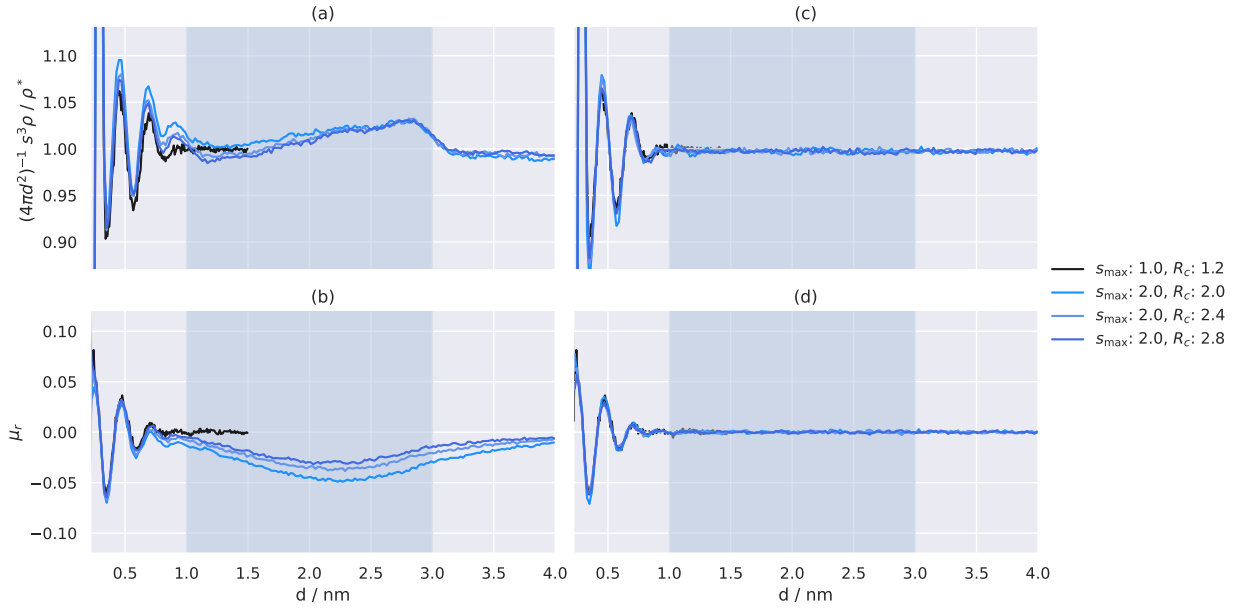

FIG. 4: Scaled density and orientational profiles around the central water molecule in spherical geometry along the distance to the box center $d = aL$. The top row shows the density distribution using AdSoS without (a) and with (c) an applied (longitudinal and orientational) correction potentials. The bottom row shows the projection of the dipole moment vector onto the scaling axis μ_r (Eq. (21)) using AdSoS without (c) and (d) with an applied (longitudinal and orientational) correction potentials. The central molecule is positionally restrained at $d = 0$ in the FG region. The shaded blue vertical strip marks the SG region.

Figs. 4a and 4b show spurious fluctuations in the local density and polarization, similar to those observed in slab geometry in the absence of a correction potential (Figs. 2a and 3a). Figs. 4c and 4d show that here also, the application of the correction procedure eliminates the artifacts. It also improves the alignment of the RDF peaks. The weights $w_{\rho,k}$ and $w_{\mu,k}$ as well as U_ρ and Φ_μ are shown in Suppl. Mat. Figs. S5-S8.

B. Interaction Energy and Relaxation Time of Water

The electrostatic and van der Waals components of the interaction energy of the central FG water molecule with its surroundings, as well as its first and second rotational relaxation times, are reported in Table II for the different AdSoS setups in spherical geometry. The corresponding autocorrelation functions of the OH bonds are shown in Suppl. Mat. Figs. S9-S10.

s_{max}	R_c [nm]	bias	U_{ele} [kJ mol^{-1}]	U_{vdw} [kJ mol^{-1}]	τ_1^{OH} [ps]	τ_2^{OH} [ps]
1.0	1.0	No	-96.7(2)	14.19(7)	3.2	1.6
	1.2	No	-97.0(2)	14.11(6)	3.8	1.8
	1.4	No	-97.3(2)	14.12(6)	3.8	1.9
	2.4	No	-97.5(2)	14.04(7)	3.9	1.9
2.0	2.0	No	-100.6(2)	14.90(8)	5.0	2.5
		Yes	-100.0(2)	14.67(6)	5.3	2.5
	2.4	No	-99.3(2)	14.62(8)	4.3	2.2
		Yes	-98.7(2)	14.39(6)	4.4	2.2
	2.8	No	-98.6(2)	14.38(7)	3.9	2.1
		Yes	-98.2(2)	14.19(7)	3.9	2.0

TABLE II: Electrostatic U_{ele} and van der Waals U_{vdw} interaction energies of the central FG water molecule with its surroundings, and its rotational relaxation times τ_1^{OH} and τ_2^{OH}. R_c is the cutoff radius. Numbers in parentheses indicate the error estimate on the energy (last digit), which was calculated using block-averaging.

The solute-solvent interaction energies are in good agreement with the FG reference. The residual differences are predominantly influenced by the choice of cutoff (rather than by the presence or absence of the correction potentials). A significant cutoff dependence is also observed for the rotational relaxation times. The values of τ_1^{OH} and τ_2^{OH} for the scaled systems converge to the FG reference when the cutoff is sufficiently large. The experimental value for τ_2^{OH} is 1.95 ps for water,[116] which is in good agreement with the large-cutoff limit of the FG reference.

C. Conformational Properties of Aqueous Alanine Dipeptide

The conformational properties of aqueous alanine dipeptide in the AdSoS scheme under spherical geometry can be compared to the FG reference based on the Ramachandran map of the backbone ϕ and ψ torsional angles (Fig. 5a). The three simulation schemes are in excellent agreement, which suggests that the conformational properties of the solute are adequately captured in the Ad-

SoS setup. Note that transitions to the left-handed helix were never observed within the 100 ns simulation times for all setups. A much longer simulation time might be necessary to cross this barrier.[117]

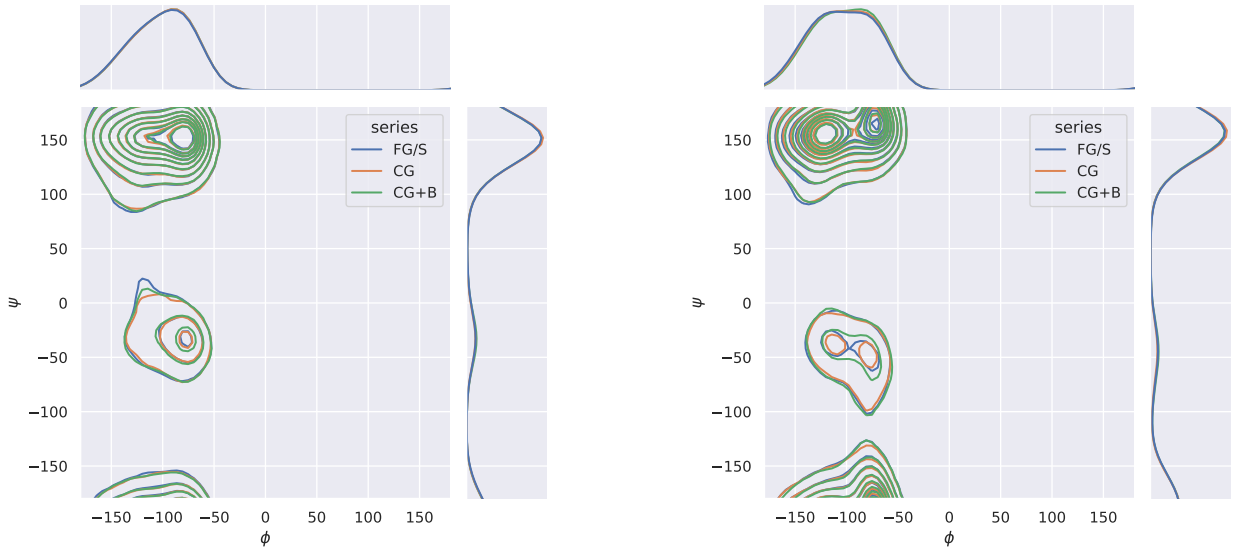

(a) Neutral peptide

(b) Zwitterionic peptide

FIG. 5: Ramachandran maps of capped alanine dipeptides from 100 ns simulations in water, after smoothing with a Gaussian kernel density estimator. The zwitterionic peptide has artificial charges of $\pm 1e$ on its terminal methyl groups. Projections of the histogram onto the individual angles are shown in the margins. The CG system (orange) refers to $s_{\max} = 2.0$ and R_c = 2.4 nm. The CG+B system (green) has the same parameters as the CG system with the additional correction potential. The FG reference setup (blue) consisted of a small box of 3 nm edge length with R_c = 1.4 nm.

To investigate the effect of net charges and thus, longer-ranged solvation effects, an artificially constructed alanine dipeptide with $q = \pm 1$ e at its terminal methyl groups was also considered. The resulting Ramachandran map is are shown in Fig. 5b. Again, no significant differences to the FG reference were observed. In both cases, the differences between AdSoS (large box volume) and FG (much smaller box volume) are also very small, which suggests that long-range effects are rather unimportant for these systems (even in the charged zwitterionic case).

D. Single Ion Hydration

The radial distribution functions around the Na^+ and Cl^- ions in water, as well as the projected dipole moment of the solvent μ_r (Eq. (21)), are shown in Fig. 6.

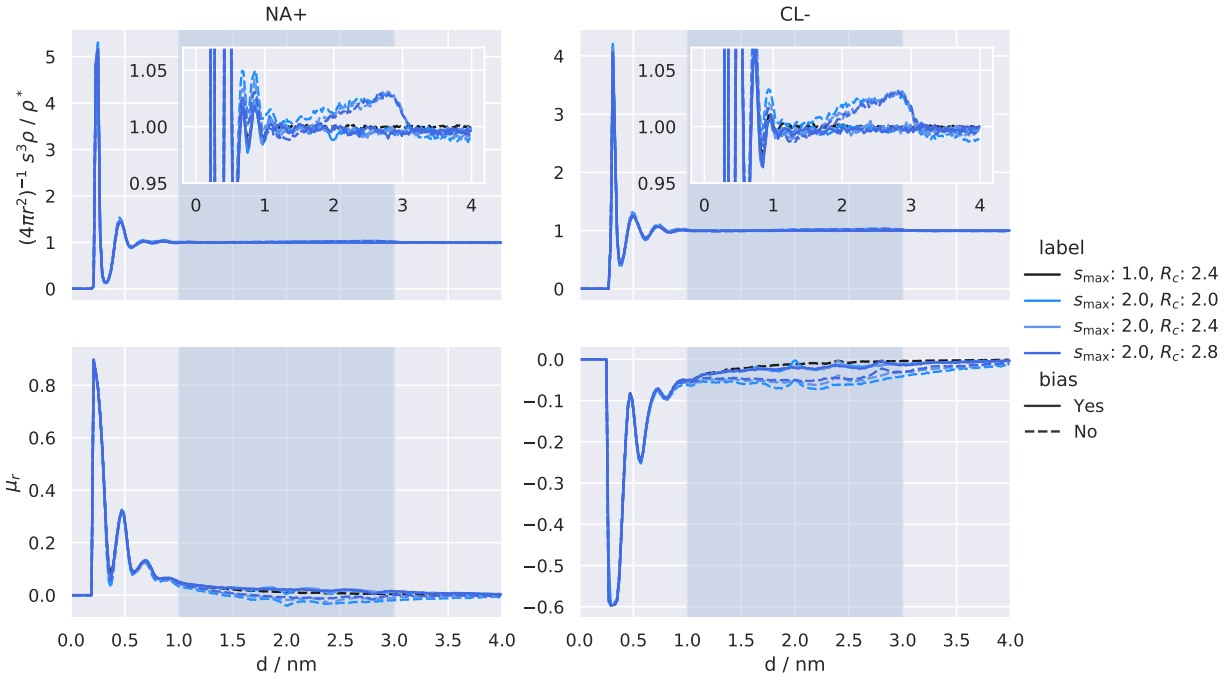

FIG. 6: Density and orientation profiles of water molecules along the scaling axis $d = aL$, with the Na^+ (left) and Cl^- ions (right) at the box center ($d = 0.0$). (Top): Scaled radial distribution function of the given ion. (Bottom): Mean projection of the dipole moment vector onto the scaling axis. The black line shows the corresponding distributions of the FG reference system with R_c = 2.4 nm. The blue lines represent a setup with $s_{\max} = 2.0$ with (solid lines) or without (dashed lines) the (longitudinal and orientational) correction potential. Different shades of blue correspond to different cutoffs.

Similar to the RDF of a central water molecule (Figs. 4a and b), the density fluctuations around the ions are short-ranged and largely limited to the FG region. However, the solvent polarization induced by the ions decays over a much longer distance. When the correction potentials are applied, a good agreement of μ_r with the FG reference can be reached. The small dents in μ_r at R_c (2.0, 2.4, or 2.8 nm for the respective systems) are likely artifacts from the group-based cutoff scheme. The same effect is observed for the FG scheme to a smaller extent. It has been shown[118–120] that the group-based cutoff scheme does not reproduce well the distance-dependent

Kirkwood factors for solvents with a high permittivity. The scaling of the dipole moment vector with $s^{3/2}$, as well as the lower degree of statistical averaging in the SG and CG regions, might further amplify the existing artifact.

The ion-solvent electrostatic interaction energies U_{ele} and their Coulomb-corrected counterparts $U_{\mathrm{ele}}^{\mathrm{corr}}$ according to Eq. (27) are shown in Fig. 7. The corresponding van der Waals energies are shown in Suppl. Mat. Fig. S11.

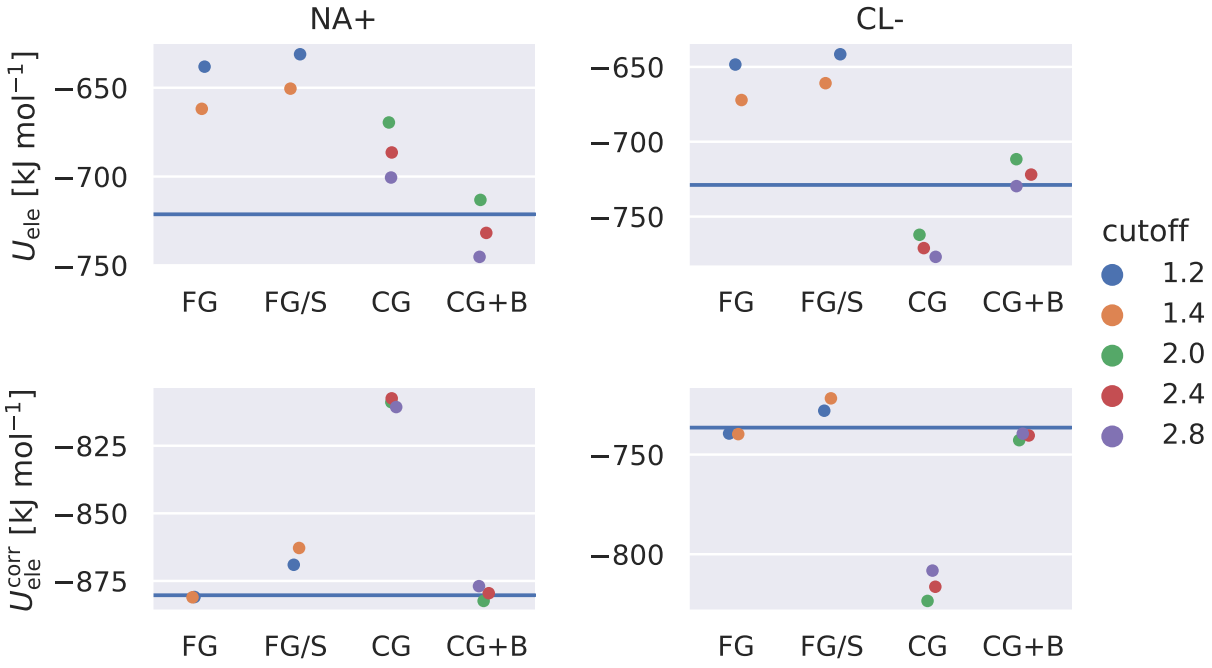

FIG. 7: Ion-solvent electrostatic interaction energies evaluated for Na^+ and Cl^- with different scaling factors and biasing schemes: "FG" is the FG system in the large box (L = 8 nm) with cutoff R_c = 1.2 or 1.4 nm, "FG/S" is the same FG system in the small box (L = 3 nm), "CG" is the AdSoS system with $s_{\mathrm{max}} = 2.0$ and cutoffs R_c = 2.0, 2.4 or 2.8 nm without correction potentials, "CG+B" is the same CG system with the correction potentials. (Top): Raw energies from the Coulomb reaction-field scheme in Eq. (6). (Bottom): Corrected energies according to Eq. (27). The horizontal blue lines correspond to the FG reference with R_c = 2.4 nm.

The uncorrected energies show a much stronger cutoff-dependence compared to those of a water molecule (Table II), because the net charge on the ions induces a long-ranged polarization of the solvent. The correction for the Coulomb interactions from Eq. (27) accounts for this effect and leads to a much better agreement of the FG and CG+B schemes, with a maximum energy difference of about 5 kJ mol^{-1}. The FG/S scheme shows more significant deviations due to finite-

size effects, which are not accounted for by Eq. (27).

An important observation concerning Fig. 7 is that the use of the correction potentials is crucial for obtaining correct ion-solvent interaction energies, even though the density and orientational artifacts in Fig. 6 have a similar magnitude as for a neutral system. The non-vanishing long-range polarization of the solvent around an ion contributes significantly contribution to its potential energy, and is more sensitive to small fluctuations in the RDF and dipole orientations around the ion.

Fig. 8 shows the calculated charging free energies ΔG of Na^+ and Cl^-. The corresponding numerical values are listed in Suppl. Mat. Table S1.

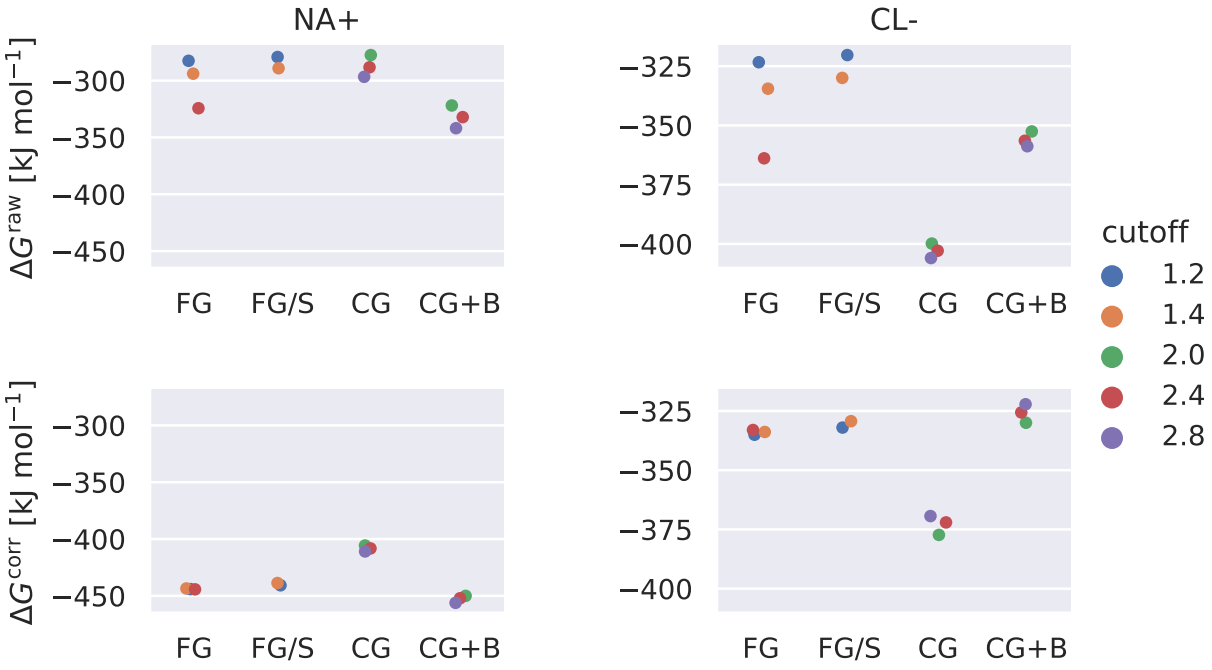

FIG. 8: Solvation free energies evaluated for Na^+ and Cl^- with different scaling factors and correction potentials: "FG" is the FG system in the large box (L = 8 nm) with cutoff R_c = 1.2 or 1.4 nm, "FG/S" is the same FG system in the small box (L = 3 nm), "CG" is the AdSoS system with $s_{\max} = 2.0$ and cutoffs R_c = 2.0, 2.4, or 2.8 nm without correction potentials, "CG+B" is the same CG system with the correction potentials. (Top): Raw solvation free energies from the Coulomb reaction-field scheme in Eq. (26). (Bottom): Corrected free energies according to Eq. (25).

The quantity ΔG^{raw} was obtained from direct integration of the electric potential (see Suppl. Mat. Figs. S12 and S13). As expected, the results are not consistent between setups with different

box sizes and cutoffs. After applying the free-energy correction to ΔG^{raw}, which accounts for both non-Coulombic and finite-size effects, the agreement between the FG, FG/S and CG+B schemes improves substantially. The maximum deviation between the CG+B and FG results is about 12 kJ mol^{-1}. However, these results differ from the solvation free energies calculated under NPT conditions with P = 1 bar, which lead to ΔG^{corr} = -465.0 kJ/mol and -283.4 kJ/mol for Na^+ and Cl^-, respectively.[115] The reported NVT simulations exhibit a significant underpressure due to electrostriction. The scaling of the compressibility with s^3 might dampen this effect in the CG region by allowing the solvent molecules to get closer to the ions, which may explain why, for both ions, the solvation free energies calculated with the CG+B scheme are closer to the NPT results than those for the FG and FG/S schemes. The experimentally determined hydration free energies are -420.2 kJ mol^{-1} and -307.8 kJ mol^{-1} for Na^+ and Cl^-, respectively.[121]

E. Polarization of Water in Presence of Multivalent Ions

The projected dipole moment of the solvent μ_r around the Na^{2+}, Na^{3+}, Cl^{2-}, and Cl^{3-} ions is shown in Fig. 9. For comparison, the μ_r calculated from the Born model is also displayed, starting at $d = 1$ nm from the ion (where $g(r)$ is close to 1) according to Eqs. (29) and (30). Similarly to the case of the monovalent ions (Fig. 6), the density profiles of the AdSoS systems are found to be in good agreement with the FG system (data not shown). It can be seen in Fig. 9 that the short-range polarization of the FG and AdSoS systems match very well. However, in the SG and CG regions, the AdSoS water is slightly overpolarized, and this trend becomes more pronounced upon increasing the charge of the central ion. The scaling of the dipole moment with $s^{3/2}$ may explain an increased interaction of the scaled water with the ion. Nevertheless, the discrepancy remains small ($< 5\%$), as the polarization decays to a significant degree in the FG region. The FG polarization, on the other hand, is in good agreement with the analytical Born polarization, and the residual discrepancies are likely due to the use of a cutoff.

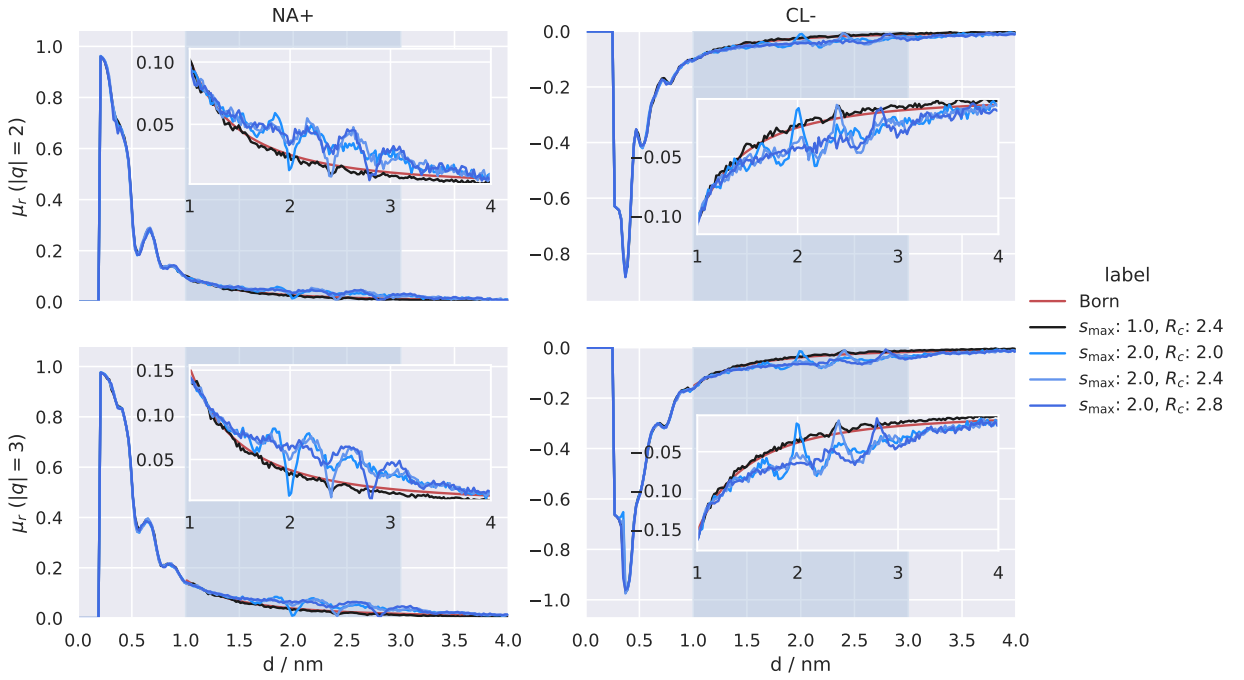

FIG. 9: Mean projection of the dipole moment vector onto the scaling axis $d = aL$, with the Na^+ (left) and Cl^- ions (right) at the box center ($d = 0.0$). The net charge of the ions in the upper row is $\pm 2e$ (*i.e.* Na^{2+} and Cl^{2-}), and $\pm 3e$ in the bottom row (*i.e.* Na^{3+} and Cl^{3-}). The black line shows the corresponding distributions of the FG reference system with R_c = 2.4 nm. The blue lines represent a setup with $s_{\max} = 2.0$ with the (longitudinal and orientational) correction potential. Different shades of blue correspond to different cutoffs.

F. Ion Pairs in AdSoS Water

Fig. 10 shows the distributions of distances between two monovalent sodium ions in AdSoS simulations (in presence of the correction potentials), expressed as a probability density. In this setup, the first ion is constrained to the box center (d = 0), while the second ion is restrained relative to the first ion using a flat-bottom half-harmonic distance restraint, starting at d = 1 nm. The latter restraint is applied in order to prevent the mobile ion from leaving the FG region, as AdSoS does not guarantee the conservation of correct charge-charge interactions between ions at different scalings. The time series of the distances are provided in Suppl. Mat. Figs. S14-S16, which show that the like-charged simulations are well converged, whereas much fewer transitions are observed for the oppositely charged ion pair, suggesting a lower reliability of the derived observables.

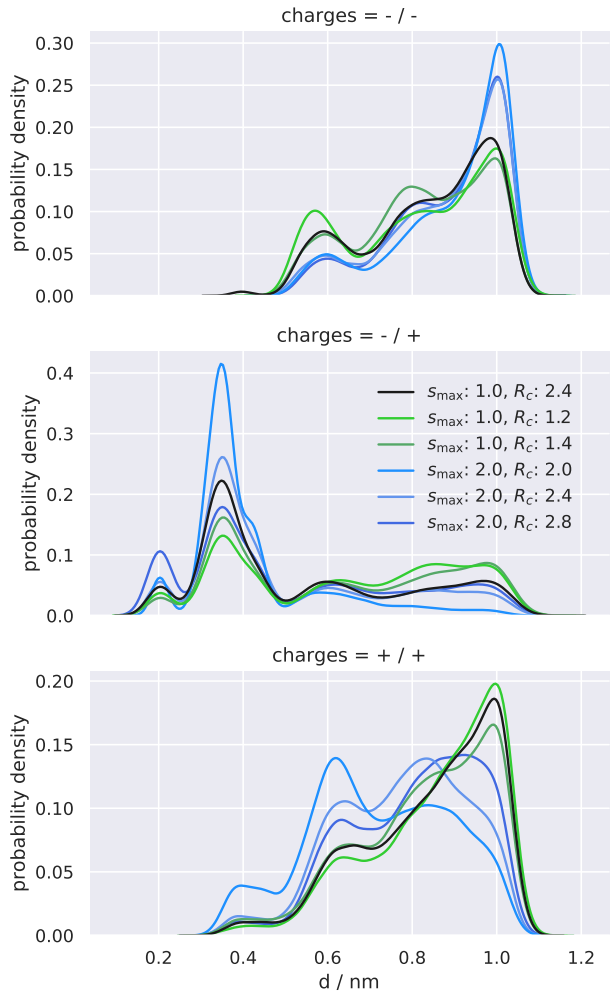

FIG. 10: Histogram of the distances between pairs of Na ions in a box with a spherical AdSoS gradient (top: Na^-/Na^-, center: Na^-/Na^+, bottom: Na^+/Na^+). The first ion is constrained to the center of the box, while the second ion is subjected to a flat-bottom half-harmonic restraint to the center ion starting at $d = 1$ nm (which coincides with the start of the SG region). The black line shows the corresponding distributions of the FG reference system with $R_c = 2.4$ nm. The green lines show two more FG setups with a smaller cutoff (1.2 and 1.4 nm, respectively). The blue lines represent a setup with $s_{\max} = 2.0$ with the (longitudinal and orientational) correction potential. Different shades of blue correspond to different cutoffs.

In case of a like-charged ion pair (Na^+/Na^+ and Na^-/Na^-, respectively), the ions aim at minimizing the electrostatic repulsion, which is reflected by a maximum in the probability distributions at 1 nm. For the oppositely charged Na^-/Na^+ ion pair, the maximum of the distribution is located at about 0.3 nm. Comparing the AdSoS simulations with the FG reference, one observes signif-

icant deviations in all cases, which are most pronounced for the positive ion pair. The cutoff is likely to represent a key factor contributing to these deviations, as it affects not only the AdSoS distributions (blue lines in Fig 10), but also causes discrepancies between FG simulations with different cutoffs (green and black lines in Fig. 10). The presence of a second ion in the box breaks the spherical symmetry, so that the forces exerted by the environment on each of the ions depend on the direction of their connecting vector. In the case of the FG system, the assumption of a homogeneous dielectric medium outside the cutoff (underlying the reaction-field method) is no longer valid. Therefore, differences arise even for the FG systems with different cutoffs. A similar effect is also in principle possible for the long-range Lennard-Jones interactions. The AdSoS approach also introduces another source of error, which is a dependence of the magnitude of the interactions at (and beyond) the cutoff on the scaling. A finding which supports this hypothesis is the decreasing deviation of the AdSoS distributions relative to the FG reference with increasing cutoff in Fig. 10. Further investigations will be required to gain a better understanding of the influence of the cutoff in AdSoS, and the development of an adaptive cutoff scheme may be necessary to improve the reliability of AdSoS in an asymmetric setup.

G. Computational Efficiency

The main motivation for the design of the AdSoS scheme is a performance improvement following from a large reduction in the number of solvent molecules in the system. This speed gain is reflected by the simulation timings, which are shown in Fig. 11 as a function of the number P of processors. Note that the FG, CG, and CG+B scheme share the same box size, but the AdSoS systems differ from the FG system in the number of molecules.

The GROMOS MD engine makes use of specialized routines to accelerate simulations of aqueous systems with the SPC water model.[108] The AdSoS scheme was implemented in a similar fashion. The group-based cutoff truncation allows for the calculation of the non-bonded interactions on the basis of entire molecules instead of atoms, and the SPC parameters were hardcoded. Since the calculation of the correction potentials, which act on all particles, is computationally demanding, a parallelization of the LEUS routine using MPI was introduced, alongside the existing distributed-memory routines for the non-bonded interactions and the SHAKE algorithm for the solvent. To this purpose, a LEUS instance was initialized on each processor and assigned N/P particles, which are coupled to this potential. The CG and CG+B schemes show a comparable

performance for up to 16 processors (Fig. 11). Increasing the number of cores further, the tasks become more and more fine-grained, and the timings become dominated by the communication overhead. The pairwise interaction calculation benefits from additional resources up to 48 processors until the performance saturates. The CG box exhibits a linear scaling with up to 8 cores, which is an inherent limitation to the scaling of GROMOS for comparable numbers of atoms.

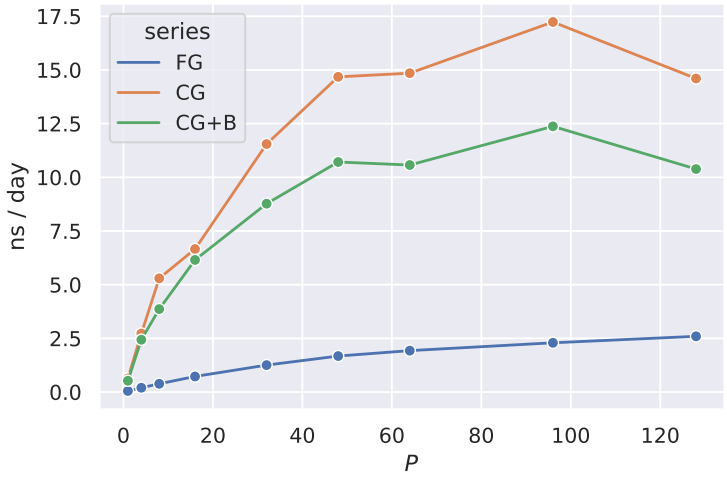

FIG. 11: Comparison of timings for the FG (with R_c = 1.4 nm), CG and CG+B schemes (both with R_c = 2.4 nm) as a function of the number P of processors. The values are extrapolated from simulations with 10^4 steps to the unit of nanoseconds per day. The calculations were performed on AMD EPYC 7742 CPUs (2.6 GHz) on the ETH HPC cluster Euler.

H. Future Developments

The solvent-scaling scheme is so far only developed for constant-volume (NVT) simulations. Due to the presence of the gradient-dependent drift forces, the pressure is not a well-defined quantity of the system. In our previous work,[82] we showed that the drift forces uphold a pressure gradient in the box according to $P(s) = s^{-3}P^*$, which suggests that the average pressure of the system is not meaningful. To be able to calculate accurate free-energy differences at constant pressure, an extension of the method to NPT conditions is crucial. A possible avenue would be to rely on a coupling involving solely the pressure of the FG region, which can be calculated using the volume-averaging method.[122] The implementation of this approach will also require an adaptation of the biasing procedure to NPT simulations.

Another shortcoming of the current method is the size requirement on the boxes to provide

a smooth transition from the FG to the CG model. With the correction potentials to cancel the interface artifacts, smaller SG regions may be explored in the future, so as to further increase the performance. For the AdResS scheme, it was shown that the hybrid region (equivalent to the SG region in the AdSoS scheme) can be completely eliminated upon application of the thermodynamic force to correct for density fluctuations.[65] Note, however, that AdSoS handles the SG region more efficiently than AdResS, as it does not require the evaluation of two separate Hamiltonians.

It should also be straightforward to extend the AdSoS setup in spherical geometry to an ellipsoidal boundary within a rectangular box. An asymmetric box partitioning would be better suited for non-spherical (*e.g.* elongated) solutes, in combination with roto-translational constraints to prevent them from escaping or protruding outside the FG region. Finally, the possible use of an adaptive cutoff (*i.e.* depending on s_i and s_j) could be explored, *e.g.* by using alternative combination rules.

Finally, it may also be of interest to investigate the applicability of lattice-sum methods[123] (Ewald[124] or particle-mesh[125–128]) in AdSoS. These approaches would incorporate long-range effects (in an artificially periodic rather than mean-field fashion[119]), while formally eliminating the dependence of the results on a truncation cutoff, the selection of which is ambiguous. However, the choice of a real-space cutoff and, for particle-mesh methods, of a reciprocal-space grid spacing leading to fast convergence would remain problematic (different requirements for the FG and CG regions).

V. CONCLUSIONS

The AdSoS method is a novel adaptive-resolution scheme, which distinguishes itself from previous approaches by relying on a continuum of CG models of increasing graining levels, that are entirely defined by a scaling of the reference FG model. Thus, the increase in graining is not obtained by grouping atoms or molecules into beads, but by scaling the atomic parameters of the FG solvent molecules. This approach relies on the fact that in empirical term-based force fields, the potential energy is a sum of terms (*e.g.* covalent, pairwise non-bonded) each characterized by a well-defined dimensional scaling.

In this work, the applicability of this method was extended from atomic liquids (previous work) to water, by introducing a molecule-based definition of the scaling, along with the implementation of additional interactions relevant for rigid solvent molecules, such as reaction-field electrostatics

and the handling of bond constraints. Furthermore, a spherical system geometry was defined in addition to the slab geometry, which is more appropriate for solvated globular macromolecules. To address artifacts in the density and molecular orientations induced by the scaling interface, a procedure to construct correction potentials was developed based on the LEUS method. It was shown that these interfacial artifacts generally do not exceed 5% in the uncorrected case, and that that the correction procedure can be used to eliminate them (nearly) completely.

The scheme was further validated for systems with FG solutes in the AdSoS system. For neutral solutes, the interaction energies and rotational relaxation times of water, as well as the backbone ϕ,ψ-distribution of alanine dipeptide, were found to be in good agreement with the FG reference even in the absence of correction potentials. These analyses also suggest that the cutoff radius needs to be scaled with s_{max}, *i.e.* $R_c = s_{max} R_c^*$, in order to mimic a FG system with a cutoff radius of R_c^*. Timings show that a tenfold increase in speed can be achieved in the linear-scaling regime by using the AdSoS scheme to reduce the number of molecules.

In order to validate the scheme for charged solutes, solute-solvent interaction energies as well as solvation free energies were calculated for the Na^+ and Cl^- ions in water. Unlike the properties of neutral solutes, the charge-solvent interaction energies have proven very sensitive to small discrepancies in the local density or polarization. Therefore, the use of the correction scheme is crucial in this case. Applying a Coulomb correction to the energies, the FG and CG+B energies are found to be in good agreement, which suggests that the AdSoS scheme is able to reproduce solute-solvent interaction energies even for charged species. Solvation free energies ΔG^{corr} calculated with the CG+B scheme were within 12 kJ mol^{-1} from the FG reference.

The AdSoS scheme can be easily extended to small rigid solvents other than water. For each molecule, one has to choose a reference atom for the scaling, ideally a central atom. Further generalization to larger and/or flexible solvent molecules may be possible using a group-based approach, whereby different atom-groups in the solvent molecule would be associated to their own scaling factors. However, in this case, the linear scaling of the interatomic distances with preservation of the angular structure would only be guaranteed within (and not between) the fragments, and the selected groups should be kept neutral so as to prevent the creation of a solvent net charge upon scaling. In the future, the solvent-scaling will also be used not only to accelerate solute-in-solvent simulations for aqueous solutes, but also to accommodate different solvents and/or solvent mixtures.

SUPPLEMENTARY MATERIAL

Implementation details of the forces in AdSoS, the adapted SHAKE algorithm, as well as the procedures for the construction and application of the correction potentials are outlined. Plots complementing the findings in the Results section are also provided.

ACKNOWLEDGEMENTS

Financial support by the Swiss National Science Foundation (Grant no. 200021-175944) is gratefully acknowledged.

DATA AVAILABILITY

The data that support the findings of this study is available from the corresponding author upon reasonable request.

REFERENCES

[1]J. Baschnagel, K. Binder, P. Doruker, A. A. Gusev, O. Hahn, K. Kremer, W. L. Mattice, F. Müller-Plathe, M. Murat, W. Paul, S. Santos, U. W. Suter, and W. Tries, "Bridging the Gap Between Atomistic and Coarse-Grained Models of Polymers: Status and Perspectives." Adv. Polym. Sci. **152**, 41–156 (2000).

[2]F. Müller-Plathe, "Coarse-Graining in Polymer Simulations: From the Atomistic to the Mesoscopic Scale and Back." Chem. Phys. Chem. **3**, 754–769 (2002).

[3]S. O. Nielsen, C. F. Lopez, G. Srinivas, and M. L. Klein, "Coarse Grain Models and the Computer Simulation of Soft Materials." J. Phys.: Condens. Matter **16**, R481–R512 (2004).

[4]S. J. Marrink, H. J. Risselada, S. Yefimov, D. P. Tieleman, and A. H. de Vries, "The MARTINI Force Field: Coarse Grained Model for Biomolecular Simulations," J. Phys. Chem. B **111**, 7812–7824 (2007).

[5]S. C. L. Kamerlin, S. Vicatos, A. Dryga, and A. Warshel, "Coarse-Grained (Multiscale) Simulations in Studies of Biophysical and Chemical Systems." Annu. Rev. Phys. Chem. **62**, 41–64 (2011).

[6]S. Riniker, J. R. Allison, and W. F. van Gunsteren, "On Developing Coarse-Grained Models for Biomolecular Simulation: A Review." Phys. Chem. Chem. Phys. **14**, 12423–12430 (2012).

[7]M. G. Saunders and G. A. Voth, "Coarse-Graining Methods for Computational Biology." Annu. Rev. Biophys. **42**, 73–93 (2013).

[8]H. I. Ingólfsson, C. A. Lopez, J. J. Uusitalo, D. H. de Jong, S. M. Gopal, X. Periole, and S. J. Marrink, "The Power of Coarse Graining in Biomolecular Simulations." WIREs Comput. Mol. Sci. **4**, 225–248 (2014).

[9]P. Kar and M. Feig, "Coarse-Grained Modeling of Proteins." Adv. Protein Chem. Struct. Biol. **96**, 143–180 (2014).

[10]A. J. Pak and G. A. Voth, "Advances in Coarse-Grained Modeling of Macromolecular Complexes." Curr. Opin. Struct. Biol. **52**, 119–126 (2018).

[11]T. E. Gartner III and A. Jayaraman, "Modeling and Simulations of Polymers: A Roadmap." Macromolecules **52**, 755–786 (2019).

[12]N. Singh and W. Li, "Recent Advances in Coarse-Grained Models for Biomolecules and their Applications." Int. J. Mol. Sci. **20**, 3774 (2019).

[13]S. Y. Joshi and S. A. Deshmukh, "A Review of Advancements in Coarse-Grained Molecular Dynamics Simulations." Mol. Simul. **47**, 786–803 (2021).

[14]M. Levitt and S. Lifson, "Refinement of Protein Conformations using a Macromolecular Energy Minimization Procedure." J. Mol. Biol. **46**, 269–279 (1969).

[15]G. S. Ayton, W. G. Noid, and G. A. Voth, "Multiscale Modeling of Biomolecular Systems: In Serial and in Parallel." Curr. Opin. Struct. Biol. **17**, 192–198 (2008).

[16]S. O. Nielsen, R. E. Bulo, P. B. Moore, and B. Ensing, "Recent Progress in Adaptive Multiscale Molecular Dynamics of Soft Matter." Phys. Chem. Chem. Phys. **12**, 12401–12414 (2010).

[17]K. Meier, A. Choutko, J. Dolenc, A. P. Eichenberger, S. Riniker, and W. F. van Gunsteren, "Multi-Resolution Simulation of Biomolecular Systems: A Review of Methodological Issues." Angew. Chem. Int. Ed. Engl. **52**, 2820–2834 (2013).

[18]A. Kovalenko and S. Gusarov, "Multiscale Methods Framework: Self-Consistent Coupling of Molecular Theory of Solvation with Quantum Chemistry, Molecular Simulations, and Dissipative Particle Dynamics." Phys. Chem. Chem. Phys. **20**, 2947–2969 (2018).

[19]H. V. Guzman, N. Tretyakov, H. Kobayashi, A. C. Fogarty, K. Kreis, J. Krajniak, C. Junghans, K. Kremer, and T. Stuehn, "ESPResSo++ 2.0: Advanced Methods for Multiscale Molecular Simulation." Comput. Phys. Commun. **238**, 66–76 (2019).

[20]S. Riniker, A. P. Eichenberger, and W. F. van Gunsteren, "Structural Effects of an Atomic-Level Layer of Water Molecules around Proteins Solvated in Supra-Molecular Coarse-Grained Water." J. Phys. Chem. B **116**, 8873–8879 (2012).

[21]P. Sokkar, S. M. Choi, and Y. M. Rhee, "Simple Method for Simulating the Mixtures of Atomistic and Coarse-Grained Molecular Systems." J. Chem. Theory Comput. **9**, 3728–3739 (2013).

[22]H. C. Gonzalez, L. Darré, and S. Pantano, "Transferable Mixing of Atomistic and Coarse-Grained Water Models." J. Phys. Chem. B **117**, 14438–14448 (2013).

[23]J. Zavadlav, M. Nuno Melo, S. J. Marrink, and M. Praprotnik, "Adaptive Resolution Simulation of an Atomistic Protein in MARTINI Water." J. Chem. Phys. **140**, 054114 (2014).

[24]A. B. Kuhn, S. M. Gopal, and L. V. Schäfer, "On using Atomistic Solvent Layers in Hybrid All-Atom/Coarse-Grained Molecular Dynamics Simulations." J. Chem. Theory Comput. **11**, 4460–4472 (2015).

[25]O. M. Szklarczyk, N. S. Bieler, P. H. Hünenberger, and W. F. van Gunsteren, "Flexible Boundaries for Multiresolution Solvation: An Algorithm for Spatial Multiscaling in Molecular Dynamics Simulations." J. Chem. Theory Comput. **11**, 5447–5463 (2015).

[26]A. Renevey and S. Riniker, "Benchmarking Hybrid Atomistic/Coarse-Grained Schemes for Proteins with an Atomistic Water Layer." J. Phys. Chem. B **123**, 3033–3042 (2019).

[27]H. Wang and A. Agarwal, "Adaptive Resolution Simulation in Equilibrium and Beyond." Eur. Phys. J. Spec. Top. **224**, 2269–2287 (2015).

[28]A. W. Duster, C. H. Wang, C. M. Garza, D. E. Miller, and H. Lin, "Adaptive Quantum/Molecular Mechanics: What have we learned, where are we, and where do we go from here?" WIREs Comput. Mol. Sci. **7**, e1310 (2017).

[29]L. Delle Site and M. Praprotnik, "Molecular Systems with Open Boundaries: Theory and Simulation." Phys. Rep. **693**, 1–56 (2017).

[30]J. Zavadlav, S. Bevc, and M. Praprotnik, "Adaptive Resolution Simulations of Biomolecular Systems." Eur. Biophys. J. **46**, 821–835 (2017).

[31]Z. Wu, Q. Cui, and A. Yethiraj, "Driving Force for the Association of Hydrophobic Peptides: The Importance of Electrostatic Interactions in Coarse-Grained Water Models." J. Phys. Chem. Lett. **2**, 1794–1798 (2011).

[32]S. Riniker, A. P. Eichenberger, and W. F. van Gunsteren, "Solvating Atomic Level Fine-Grained Proteins in Supra-Molecular Level Coarse-Grained Water for Molecular Dynamics Simulations." Eur. Biophys. J. **41**, 647–661 (2012).

[33]W. Han and K. Schulten, "Further Optimization of a Hybrid United-Atom and Coarse-Grained Force Field for Folding Simulations: Improved Backbone Hydration and Interactions Between Charged Side Chains." J. Chem. Theory Comput. **8**, 4413–4424 (2012).

[34]Z. Lin and W. F. van Gunsteren, "Free Enthalpy Differences between α-, π-, and 3_{10}-Helices of an Atomic Level Fine-Grained Alanine Decapeptide Solvated in Supramolecular Coarse-Grained Water." J. Chem. Theory Comput. **9**, 1328–1333 (2013).

[35]M. Orsi, W. Ding, and M. Palaikostas, "Direct Mixing of Atomistic Solutes and Coarse-Grained Water." J. Chem. Theory Comput. **10**, 4684–4693 (2014).

[36]W. Huang, S. Riniker, and W. F. van Gunsteren, "Rapid Sampling of Folding Equilibria of β-Peptides in Methanol using a SupraMolecular Solvent Model." J. Chem. Theory Comput. **10**, 2213–2223 (2014).

[37]W. Huang, N. Hansen, and W. F. van Gunsteren, "On the Use of a Supramolecular Coarse-Grained Model for the Solvent in Simulations of the Folding Equilibrium of an Octa-β-Peptide in MeOH and H_2O." Helv. Chim. Acta **97**, 1591–1605 (2014).

[38]S. Genheden and J. W. Essex, "A Simple and Transferable All-Atom/Coarse-Grained Hybrid Model to Study Membrane Processes." J. Chem. Theory Comput. **11**, 4749–4759 (2015).

[39]S. Genheden, "Predicting Partition Coefficients with a Simple All-Atom/Coarse-Grained Hybrid Model." J. Chem. Theory Comput. **12**, 297–304 (2016).

[40]X. C. Yan, J. Tirado-Rives, and W. L. Jorgensen, "Hydration Properties and Solvent Effects for All-Atom Solutes in Polarizable Coarse-Grained Water." J. Phys. Chem. B **120**, 8102–8114 (2016).

[41]A. Renevey and S. Riniker, "Improved Accuracy of Hybrid Atomistic/Coarse-Grained Simulations using Reparametrised Interactions." J. Chem. Phys. **146**, 124131 (2017).

[42]T. Ichiye and M. L. Tan, "Soft Sticky Dipole-Quadrupole-Octupole Potential Energy Function for Liquid Water: an Approximate Expansion." J. Phys. Chem. **124**, 134504 (2006).

[43]P. A. Golubkov, J. C. Wu, and P. Ren, "A Transferable Coarse-Grained Model for Hydrogen-Bonding Liquids." Phys. Chem. Chem. Phys. **10**, 2050–2057 (2008).

[44]V. Molinero and E. B. Moore, "Water Modeled as an Intermediate Element Between Carbon and Silicon." J. Phys. Chem. B **113**, 4008–4016 (2009).

[45]K. R. Hadley and C. McCabe, "On the Investigation of Coarse-Grained Models for Water: Balancing Computational Efficiency and the Retension of Structural Properties." J. Phys. Chem. B **114**, 4590–4599 (2010).

[46]S. O. Yesylevskyy, L. V. Schäfer, D. Sengupta, and S. J. Marrink, "Polarizable Water Model for the Coarse-Grained MARTINI Force Field." PLoS Comput. Biol. **6**, e1000810 (2010).

[47]Z. Wu, Q. Cui, and A. Yethiraj, "A new Coarse-Grained Model for Water: The Importance of Electrostatic Interactions." J. Phys. Chem. B **114**, 10524–10529 (2010).

[48]S. Riniker and W. F. van Gunsteren, "A Simple, Efficient Polarisable Coarse-Grained Water Model for Molecular Dynamics Simulations." J. Chem. Phys. **134**, 084110 (2011).

[49]K. R. Hadley and C. McCabe, "Coarse-Grained Molecular Models of Water: A Review." Mol. Simul. **38**, 671–681 (2012).

[50]M. Orsi, "Comparative Assessment of the ELBA Coarse-Grained Model for Water." Mol. Phys. **112**, 1566–1576 (2014).

[51]R. Qi, L. P. Wang, Q. Wang, V. S. Pande, and P. Ren, "United Polarizable Multipole Water Model for Molecular Mechanics Simulation." J. Chem. Phys. **143**, 014504 (2015).

[52]M. Deng and H. Shen, "Coarse-Grained Model for Water Involving a Virtual Site." J. Phys. Chem. B **120**, 733–739 (2016).

[53]K. K. Bejagam, S. Singh, Y. An, C. Berry, and S. A. Deshmukh, "PSO-Assisted Development of New Transferable Coarse-Grained Water Models." J. Phys. Chem. B **122**, 1958–1971 (2018).

[54]P. G. Lafond and S. Izvekov, "Multiscale Coarse-Graining with Effective Polarizabilities: A Fully Bottom-Up Approach." J. Chem. Theory Comput. **14**, 1873–1886 (2018).

[55]J. Zavadlav, M. N. Melo, A. V. Cunha, A. H. de Vries, S. J. Marrink, and M. Praprotnik, "Adaptive Resolution Simulation of MARTINI Solvents." J. Chem. Theory Comput. **10**, 2591–2598 (2014).

[56]J. Zavadlav, S. J. Marrink, and M. Praprotnik, "Adaptive Resolution Simulation of Supramolecular Water: The Concurrent Making, Breaking, and Remaking of Water Bundles." J. Chem. Theory Comput. **12**, 4138–4145 (2016).

[57]J. Zavadlav, S. J. Marrink, and M. Praprotnik, "Multiscale Simulation of Protein Hydration Using the SWINGER Dynamical Clustering Algorithm." J. Chem. Theory Comput. **14**, 1754–1761 (2018).

[58]J. Zavadlav, S. J. Marrink, and M. Praprotnik, "SWINGER: A Clustering Algorithm for Concurrent Coupling of Atomistic and Supramolecular Liquids." Interface Focus **9**, 20180075 (2019).

[59]M. Praprotnik, L. Delle Site, and K. Kremer, "Adaptive Resolution Molecular-Dynamics Simulation: Changing the Degrees of Freedom on the Fly." J. Chem. Phys. **123**, 224106 (2005).

[60]M. Praprotnik, L. Delle Site, and K. Kremer, "Multiscale Simulation of Soft Matter: From Scale Bridging to Adaptive Resolution." Ann. Rev. Phys. Chem. **59**, 545–571 (2008).

[61]S. Poblete, M. Praprotnik, K. Kremer, and L. Delle Site, "Coupling Different Level of Resolution in Molecular simulations." J. Chem. Phys. **132**, 114101 (2010).

[62]M. Praprotnik, S. Poblete, and K. Kremer, "Statistical Physics Problems in Adaptive Resolution Computer Simulations of Complex Fluids." J. Stat. Phys. **145**, 946–966 (2011).

[63]S. Fritsch, S. Poblete, C. Junghans, G. Ciccotti, L. Delle Site, and K. Kremer, "Adaptive Resolution Molecular Dynamics Simulation through Coupling to an Internal Particle Reservoir." Phys. Rev. Lett. **108**, 170602 (2012).

[64]M. Praprotnik, S. Matysiak, L. Delle Site, K. Kremer, and C. Clementi, "Adaptive Resolution Simulation of Liquid Water." J. Phys. Condens. Matter **19**, 292201 (2007).

[65]C. Krekeler, A. Agarwal, C. Junghans, M. Praprotnik, and L. Delle Site, "Adaptive Resolution Molecular Dynamics Technique: Down to the Essential." J. Chem. Phys. **149**, 024104 (2018).

[66]R. Potestio, S. Fritsch, P. Espanol, R. Delgado-Buscalioni, K. Kremer, R. Everaers, and D. Donadio, "Hamiltonian Adaptive Resolution Simulation for Molecular Liquids." Phys. Rev. Lett. **110**, 108301 (2013).

[67]R. Potestio, P. Espanol, R. Delgado-Buscalioni, R. Everaers, K. Kremer, and D. Donadio, "Monte Carlo Adaptive Resolution Simulation of Multicomponent Molecular Liquids." Phys. Rev. Lett. **111**, 060601 (2013).

[68]A. Agarwal, H. Wang, C. Schütte, and L. Delle Site, "Chemical Potential of Liquids and Mixtures via Adaptive Resolution Simulation." J. Chem. Phys. **141**, 034102 (2014).

[69]P. Español, R. Delgado-Buscalioni, R. Everaers, R. Potestio, D. Donadio, and K. Kremer, "Statistical Mechanics of Hamiltonian Adaptive Resolution Simulations." J. Chem. Phys. **142**, 064115 (2015).

[70]B. Ensing, S. O. Nielsen, P. B. Moore, M. L. Klein, and M. Parrinello, "Energy Conservation in Adaptive Hybrid Atomistic/Coarse-Grain Molecular Dynamics." J. Chem. Theory Comput. **3**, 1100–1105 (2007).

[71]A. Heyden and D. G. Truhlar, "Conservative Algorithm for an Adaptive Change of Resolution in Mixed Atomistic/Coarse-Grained Multiscale Simulations." J. Chem. Theory Comput. **4**, 217–221 (2008).

[72]J. A. Wagoner and V. S. Pande, "A Smoothly Decoupled Particle Interface: New Methods for Coupling Explicit and Implicit Solvent." J. Chem. Phys. **134**, 214103 (2011).

[73]J. A. Wagoner and V. S. Pande, "Finite Domain Simulations with Adaptive Boundaries: Accurate Potentials and Nonequilibrium Movesets." J. Chem. Phys. **139**, 234114 (2013).

[74]S. Artemova and S. Redon, "Adaptively Restrained Particle Simulations." Phys. Rev. Lett. **109**, 190201 (2012).

[75]M. G. Guenza, "Advancements in Multi Scale Modeling: Adaptive Resolution Simulations and Related Issues." Eur. Phys. J. Spec. Top. **224**, 2491–2495 (2015).

[76]R. Delgado-Buscalioni, "Thermodynamics of Adaptive Molecular Resolution." Phil. Trans. R. Soc. A **374**, 20160152 (2016).

[77]R. Fiorentini, K. Kremer, R. Potestio, and A. C. Fogarty, "Using Force-based Adaptive Resolution Simulations to Calculate Solvation Free Energies of Amino Acid Sidechain Analogues." J. Chem. Phys. **146**, 244113 (2017).

[78]L. D. Site, C. Krekeler, J. Whittaker, A. Agarwal, R. Klein, and F. Höfling, "Molecular dynamics of open systems: Construction of a mean-field particle reservoir," Adv. Theory Simul. **2**, 1900014 (2019).

[79]J. Whittaker and L. D. Site, "Investigation of the hydration shell of a membrane in an open system molecular dynamics simulation," Phys. Rev. Research **1**, 033099 (2019).

[80]R. E. Viand, F. Höfling, R. Klein, and L. D. Site, "Theory and simulation of open systems out of equilibrium," J. Chem. Phys. **153**, 101102 (2020).

[81]A. Gholami, R. Klein, and L. D. Site, "Simulation of a particle domain in a continuum fluctuating hydrodynamics reservoir," Phys. Rev. Lett. **129**, 230603 (2022).

[82]A. Kubincová, S. Riniker, and P. H. Hünenberger, "Solvent-Scaling as an Alternative to Coarse-Graining in Adaptive-Resolution Simulations: The Adaptive Solvent-Scaling (AdSoS) Scheme." J. Chem. Phys. **155**, 094107 (2021).

[83]M. Heidari, R. Cortes-Huerto, D. Donadio, and R. Potestio, "Accurate and General Treatment of Electrostatics Interaction in Hamiltonian Adaptive Resolution Schemes." Eur. Phys. J. Special Topics **225**, 1505–1526 (2016).

[84]L. Delle Site and R. Klein, "Liouville-Type Equations for the n-Particle Distribution Functions of an Open System." J. Math. Phys. **61**, 083102 (2020).

[85]A. Gholami, F. Höfling, R. Klein, and L. Delle Site, "Thermodynamic Relations at the Coupling Boundary in Adaptive Resolution Simulations for Open Systems." Adv. Theory Simul. **4**, 2000303 (2021).

[86]P. Depa, C. Chen, and J. K. Maranas, "Why are Coarse-Grained Force Fields Too Fast? A Look at Dynamics of Four Coarse-Grained Polymers." J. Chem. Phys. **134**, 014903 (2011).

[87]M. K. Meinel and F. Müller-Plathe, "Loss of Molecular Roughness upon Coarse-Graining Predicts the Artificially Accelerated Mobility of Coarse-Grained Molecular Simulation Models." J. Chem. Theory Comput. **16**, 1411–1419 (2020).

[88]G. G. Rondina, M. C. Böhm, and F. Müller-Plathe, "Predicting the Mobility Increase of Coarse-Grained Polymer Models from Excess Entropy Differences." J. Chem. Theory Comput. **16**, 1431–1447 (2020).

[89]M. Praprotnik, K. Kremer, and L. Delle Site, "Adaptive Molecular Resolution via a Continuous Change of the Phase Space Dimensionality." Phys. Rev. E **75**, 017701 (2007).

[90]M. Praprotnik, K. Kremer, and L. Delle Site, "Fractional Dimensions of Phase Space Variables: A Tool for Varying the Degrees of Freedom of a System in a Multiscale Treatment." J. Phys. A Math. Theor. **40**, F281–F288 (2007).

[91]R. J. Good and C. J. Hope, "New Combining Rule for Intermolecular Distances in Intermolecular Potential Functions." J. Chem. Phys. **53**, 540–543 (1970).

[92]R. J. Good and C. J. Hope, "Test of Combining Rules for Intermolecular Distances - Potential Function Constants from Second Virial Coefficients." J. Chem. Phys. **55**, 111–116 (1971).

[93]C. A. Coulomb, "Sur l'électricité et le magnétisme, premier mémoire, construction et usage d'une balance électrique, fondée sur la propriété qu'ont les fils de métal, d'avoir une force de réaction de torsion proportionnelle à l'angle de torsion." Mémoires de l'Académie Royale des Sciences **1785**, 569–577 (1788).

[94]J. A. Barker and R. O. Watts, "Monte Carlo Studies of the Dielectric Properties of Water-like Models." Mol. Phys. **26**, 789–792 (1973).

[95]I. G. Tironi, R. Sperb, P. E. Smith, and W. F. van Gunsteren, "A Generalized Reaction Field Method for Molecular Dynamics Simulations." J. Chem. Phys. **102**, 5451–5459 (1995).

[96]J. E. Lennard-Jones, "The Equation of State of Gases and Critical Phenomena." Physica **4**, 941–956 (1937).

[97]K. Kreis and R. Potestio, "The Relative Entropy is Fundamental to Adaptive Resolution Simulations." J. Chem. Phys. **145**, 044104 (2016).

[98]K. Kreis, D. Donadio, K. Kremer, and R. Potestio, "A Unified Framework for Force-Based and Energy-Based Adaptive Resolution Simulations." EPL **108**, 30007 (2014).

[99]R. W. Hockney, "The Potential Calculation and some Applications." Methods Comput. Phys. **9**, 135–211 (1970).

[100]R. Potestio, "Computer Simulation of Particles with Position-Dependent Mass." Eur. Phys. J. B **87**, 245 (2014).

[101]J. P. Ryckaert, G. Ciccotti, and H. J. C. Berendsen, "Numerical Integration of the Cartesian Equations of Motion of a System with Constraints: Molecular Dynamics of *n*-Alkanes." J. Comput. Phys. **23**, 327–341 (1977).

[102]H. S. Hansen and P. H. Hünenberger, "Using the Local Elevation Method to Construct Optimized Umbrella Sampling Potentials: Calculation of the Relative Free Energies and Interconversion Barriers of Glucopyranose Ring Conformers in Water." J. Comput. Chem. **31**, 1–23 (2010).

[103]T. Huber, A. E. Torda, and W. F. van Gunsteren, "Local Elevation: A Method for Improving the Searching Properties of Molecular Dynamics Simulation." J. Comput.-Aided Mol. Des. **8**, 695–708 (1994).

[104]J. P. Valleau and G. M. Torrie, "A Guide to Monte Carlo for Statistical Mechanics: 1. Highways." in *Modern theoretical chemistry.*, Vol. 5, edited by B. J. Berne (Plenum Press, New York, USA, 1977).

[105]V. Babin, C. Roland, and C. Sagui, "Adaptively Biased Molecular Dynamics for Free Energy Calculations." J. Chem. Phys. **128**, 134101 (2008).

[106]N. S. Bieler, R. Häuselmann, and P. H. Hünenberger, "Local Elevation Umbrella Sampling Applied to the Calculation of Alchemical Free-Energy Changes via λ-Dynamics: The λ-LEUS Scheme." J. Chem. Theory Comput. **10**, 3006–3022 (2014).

[107]J. F. Dama, M. Parrinello, and G. A. Voth, "Well-Tempered Metadynamics Converges Asymptotically." Phys. Rev. Lett. **112**, 1–6 (2014).

[108]N. Schmid, C. D. Christ, M. Christen, A. P. Eichenberger, and W. F. van Gunsteren, "Architecture, Implementation and Parallelisation of the GROMOS Software for Biomolecular Simulation." Comput. Phys. Commun. **183**, 890–903 (2012).

[109]H. J. C. Berendsen, J. P. M. Postma, W. F. van Gunsteren, and J. Hermans, "Interaction Models for Water in Relation to Protein Hydration." in *Intermolecular Forces.*, edited by B. Pullman (Reidel, Dordrecht, The Netherlands, 1981).

[110]N. Schmid, A. P. Eichenberger, A. Choutko, S. Riniker, M. Winger, A. E. Mark, and W. F. van Gunsteren, "Definition and Testing of the GROMOS Force-Field Versions 54A7 and 54B7."

Eur. Biophys. J. **40**, 843–856 (2011).

[111]H. J. C. Berendsen, J. P. M. Postma, W. F. van Gunsteren, A. di Nola, and J. R. Haak, "Molecular Dynamics with Coupling to an External Bath." J. Chem. Phys. **81**, 3684–3690 (1984).

[112]A. P. Eichenberger, J. R. Allison, J. Dolenc, D. P. Geerke, B. A. C. Horta, K. Meier, C. Oostenbrink, N. Schmid, D. Steiner, D. Wang, and W. F. van Gunsteren, "The GROMOS++ Software for the Analysis of Biomolecular Simulation Trajectories." J. Chem. Theory Comput. **7**, 3379–3390 (2011).

[113]M. M. Reif and P. H. Hünenberger, "Computation of Methodology-Independent Single-Ion Solvation Properties from Molecular Simulations. III. Correction Terms for the Solvation Free Energies, Enthalpies, Entropies, Heat Capacities, Volumes, Compressibilities and Expansivities of Solvated Ions." J. Chem. Phys. **134**, 144103 (2011).

[114]M. Born, "Volumen und Hydrationswärme der Ionen." Z. Phys. **1**, 45–48 (1920).

[115]M. M. Reif and P. H. Hünenberger, "Computation of Methodology-Independent Single-Ion Solvation Properties from Molecular Simulations. IV. Optimized Lennard-Jones Parameter Sets for the Alkali and Halide Ions in Water." J. Chem. Phys. **134**, 144104 (2011).

[116]R. Ludwig, "NMR Relaxation Studies in Water-Alcohol Mixtures: the Water-Rich Region," Chem. Phys. **195**, 329 (1995).

[117]F. Vitalini, F. Noé, and B. G. Keller, "Molecular Dynamics Simulations Data of the Twenty Encoded Amino Acids in Different Force Fields." Data in Brief **7**, 582–590 (2016).

[118]P. H. Hünenberger and W. F. van Gunsteren, "Alternative Schemes for the Inclusion of a Reaction-Field Correction into Molecular Dynamics Simulations: Influence on the Simulated Energetic, Structural, and Dielectric Properties of Liquid Water." J. Chem. Phys. **108**, 6117–6134 (1998).

[119]A. Kubincová, S. Riniker, and P. H. Hünenberger, "Reaction-Field Electrostatics in Molecular Dynamics Simulations: Development of a Conservative Scheme Compatible with an Atomic Cutoff." Phys. Chem. Chem. Phys. **22**, 26419–26437 (2020).

[120]M. Diem and C. Oostenbrink, "The Effect of Different Cutoff Schemes in Molecular Simulations of Proteins." J. Comput. Chem. **16**, 5985–5990 (2020).

[121]P. H. Hünenberger and M. M. Reif, *Single-Ion Solvation: Experimental and Theoretical Approaches to Elusive Thermodynamic Quantities.*, 1st ed. (Royal Society of Chemistry (Theoretical and Computational Chemistry Series), London, UK, 2011).

[122]J. F. Lutsko, "Stress and Elastic Constants in Anisotropic Solids: Molecular Dynamics Techniques," J. Appl. Phys. **64**, 1152–1154 (1988).

[123]P. H. Hünenberger, "Lattice-sum methods for computing electrostatic interactions in molecular simulations." in *Simulation and theory of electrostatic interactions in solution: Computational chemistry, biophysics, and aqueous solution.*, Vol. 492, edited by G. Hummer and L. R. Pratt (American Institute of Physics, New York, USA, 1999).

[124]P. P. Ewald, "Die Berechnung optischer und elektrostatischer Gitterpotentiale." Ann. Phys. **369**, 253–287 (1921).

[125]R. W. Hockney and J. W. Eastwood, *Computer simulation using particles.* (McGraw-Hill, New York, USA, 1981).

[126]R. W. Hockney and J. W. Eastwood, *Computer simulation using particles.*, 2nd ed. (Institute of Physics Publishing, Bristol, UK, 1988).

[127]T. Darden, D. York, and L. Pedersen, "Particle mesh Ewald: An Nlog(N) method for Ewald sums in large systems." J. Chem. Phys. **98**, 10089–10092 (1993).

[128]U. Essmann, L. Perera, M. L. Berkowitz, T. Darden, H. Lee, and L. G. Pedersen, "A smooth particle mesh Ewald method." J. Chem. Phys. **103**, 8577–8593 (1995).